International Journal of Hydrogen Energy 57 (2024) 1229–1243

Contents lists available at ScienceDirect

International Journal of Hydrogen Energy

journal homepage: www.elsevier.com/locate/he

An Arrhenius-based one-step reaction mechanism for hydrogen-air flames simulations in an extended range of operating conditions

Francesco G. Schiavone [a,*], Nicola Detomaso [b], Marco Torresi [a], Davide Laera [a]

[a] Department of Mechanics, Mathematics and Management, Polytechnic University of Bari, Via Orabona 4, Bari, 70125, Italy
[b] CERFACS, 42 avenue Gaspard Coriolis, Toulouse, 31057, France

ARTICLE INFO

Keywords:
Hydrogen
Combustion
Global reaction mechanism
Numerical simulations
Premixed flames
Expanding flames

ABSTRACT

An Arrhenius-based one-step scheme is derived for hydrogen-air combustion simulations. A Pre-Exponential Adjustment approach, based on an explicit analytical dependence of reaction rate parameters on equivalence ratio and pressure is adopted, together with a correction to improve the prediction of thermal flame thickness. The reduced scheme is validated by computations of one-dimensional unstrained and strained laminar premixed flames for a wide range of pressures ([1; 30] atm), unburned gas temperatures ([300; 800] K), and equivalence ratios ([0.4; 6.0]), with a good agreement of predicted main flame parameters between reduced and reference kinetic schemes. Coupled to a high-fidelity Navier–Stokes compressible solver, the reduced scheme is successfully proved for the numerical simulation of canonical configurations such as one-dimensional and two-dimensional premixed flames under several mixture conditions, with a significant improvement of computational efficiency.

1. Introduction

The hydrogen role in the current global energy transition process has been recognized both by the scientific community (e.g., the International Energy Agency [1]) and the national governments to complement power supply from renewable energy sources [2]: as a carbon-free species, it is recently gaining momentum as a possible fuel to reduce carbon dioxide (CO_2) emissions [3]. Several applications of hydrogen combustion have been considered, both in the power generation (e.g., hydrogen-fueled gas turbines [4,5]) and transportation sectors (e.g., hydrogen-fueled aircraft [6] and internal combustion engines [7,8]). Nevertheless, the exploitation of hydrogen in industrial combustion processes remains an open field of study [9], due to challenging technical issues (e.g., potential flashback [10], autoignition [11], safety [12], and storage [13]), and its peculiar physicochemical properties, such as wide flammability range [14], large flame propagation speed [15], and small quenching distance [16].

The complex phenomena characterizing hydrogen as a fuel make Computational Fluid Dynamics (CFD) an indispensable tool to analyze such flames in different conditions of interest. Nevertheless, numerical simulations of hydrogen combustion require an additional effort, since most of the existing models, developed for hydrocarbons, may not be appropriate [17]. Therefore, albeit the full kinetics of hydrogen oxidation is well-known and significantly simpler than hydrocarbons', its integration into CFD calculations is challenging, especially for three-dimensional simulations of real systems, where computational costs can easily become unsustainable [18].

Considering the computational benefits that can be obtained from a reduced number of species and reactions in the numerical code, a significant effort has been put into the derivation of effective and sufficiently accurate simplified descriptions of chemical mechanisms, with different approaches. Wang et al. [19] proposed a reduced mechanism relying on tabulated activation energy factor to predict ignition for a wide range of operating conditions (i.e., excess air coefficients between 0.56 and 8.4, unburned mixture temperatures between 850 and 1800 K, and pressures between 0.1 and 100 atm). Nevertheless, tabulated chemistry methods generally require the use of expensive algorithms for efficiently storing and searching out data in tables [20], and may be challenging in case of multi-regime flames, often characterizing hydrogen-fueled systems [21], due to the great difficulty in choosing the correct reference canonical configuration.

Two other main routes can be considered to achieve global or semi-global chemistry descriptions. First, the reaction rate can be analytically described by means of first-principles-derived approaches, such as the quasi-steady-state (QSS) approximation. In this sense, a two-step reduced mechanism for premixed hydrogen flames was proposed by Mauss et al. [18], based on the QSS approximation for O, OH

* Corresponding author.
E-mail address: f.schiavone11@phd.poliba.it (F.G. Schiavone).

https://doi.org/10.1016/j.ijhydene.2023.12.301
Received 26 September 2023; Received in revised form 17 December 2023; Accepted 31 December 2023
Available online 18 January 2024

and HO_2 radicals, and a three-step overall scheme was systematically derived from the San Diego mechanism [22] by Boivin et al. [23], by applying the QSS approximation to O, OH and H_2O_2 radicals and introducing a correction factor to better predict autoignition in lean and stoichiometric flames. More recently, the QSS approach was extended to the H-radical, so that a one-step reduced mechanism for hydrogen-air combustion was systematically derived [24–26]. This approach is certainly attractive, given its rigorous formalism, especially when dealing with ultra-lean flames, as it may occur for example in gas turbine applications. Indeed, as observed in [20], the application of the steady-state hypothesis for the H-radical is strictly valid only near the lean flammability limit, where radical concentrations assume very low values, slowing down the direct recombination reactions. Nevertheless, two main drawbacks, possibly affecting its applicability, can be identified. From a technical point of view, the implementation of this non-Arrhenius-based reaction rate description in existing numerical simulation codes may be challenging. Moreover, a single overall irreversible reaction $2\,H_2 + O_2 \longrightarrow 2\,H_2O$ coupled with the QSS approach is strictly valid only for narrower temperature ranges [26].

On the other hand, reduced mechanisms can be derived based on a "best-fit" targeting of reaction rate parameters to match detailed kinetics or experimental results. Coffee et al. [27,28] proposed stoichiometry-dependent Arrhenius-based reaction rate parameters for a single overall irreversible reaction, relying on a least squares fit of the heat release rate profiles obtained from detailed kinetics. Marinov et al. [29] determined a global rate expression for hydrogen-air combustion, based on the single global reversible reaction $H_2 + \frac{1}{2}\,O_2 \rightleftharpoons H_2O$. This model, however, correctly reproduces detailed chemistry behavior only at atmospheric pressure and for $0.55 < \phi < 1.1$. Wang et al. [30], adapting the methodology proposed in [31], developed a global mechanism to predict the deflagration-to-detonation transition in an obstructed channel, with appreciable numerical results for the operating condition investigated. Bar-Kohany and Dahan [32] employed a global one-step kinetics description in CFD simulations to predict autoignition limits. More recently, Kim and Kim [33] proposed one-step global reaction mechanisms for different fuels, including hydrogen, and compared the laminar burning velocity, derived from one-dimensional unstretched laminar premixed flame calculations, with values from detailed reaction mechanisms, showing a good agreement for various equivalence ratios, ranging from lean ($\phi = 0.5$) to rich ($\phi = 5.0$) conditions, at 300 K and 1 bar, as well as for moderate temperature variations up to 600 K; nevertheless, both pressure and stretch effects were not considered in their derivation. All the mentioned works provide reasonably good descriptions of hydrogen oxidation for specific flame conditions, requiring an updating of parameters when initial mixture conditions are modified. To the best of our knowledge, differently from what has been done for common hydrocarbons (e.g., [34]), there is a lack in the literature for an Arrhenius-based global reaction mechanism able to capture the main properties of hydrogen-air flames in a sufficiently wide range of conditions. Albeit the importance of complex chemistry is indisputable and the accuracy of global reaction schemes remains restricted, computational costs reasons make simplified chemical descriptions essential.

Based on these premises, the present work aims to exploit the numerical simplicity of the best-fitting approach to construct a one-step reduced mechanism able to describe the main properties of hydrogen-air flames (i.e., laminar flame speed, laminar flame thickness, adiabatic flame temperature, and flame response to stretch) for a various set of initial conditions of the reactants, both in terms of mixture composition (i.e., equivalence ratio) and thermodynamic state (i.e., unburned gas temperature and pressure). Simple expressions are adopted for the reaction rate adjustment functions, and the terms depending on pressure and equivalence ratio are explicitly decoupled, to preserve the computational efficiency of the reduced scheme. The reduced mechanism is validated against a detailed scheme for a wide range of equivalence ratios ([0.4; 6.0]), pressures ([1; 30] atm), and unburned gas temperatures ([300; 800] K), by computing well-known canonical premixed flames, both one- and two-dimensional. The reduced scheme is also implemented in a DNS/LES code, proving to be a valid solution for CFD simulations to optimize computational resources when preliminary and less expensive computations are required.

2. Derivation of the global reaction mechanism

A combustible mixture of given temperature, pressure and composition is characterized by three fundamental properties, namely the adiabatic flame temperature T_{ad}, the laminar burning flux m^0 (i.e., the product of unburned mixture density ρ_u and laminar flame speed S_L^0), and the laminar flame thickness δ_L^0. Moreover, in the case of stretched flames, the sensitivity of the laminar flame to the combined effects of stretch and nonequidiffusion is also to be considered [35,36]. A reduced mechanism should be able to capture, with sufficient accuracy, these properties in the widest possible range of initial temperatures, pressures and compositions. For the present work, the one-step reaction mechanism is developed based on the accurate prediction of the laminar flame speed (and, consequently, of the burning flux); nevertheless, adjustments in the transport properties of the mixture are introduced so that also the other main flame properties can be predicted with sufficient accuracy.

In this work, the San Diego mechanism (UCSD) [22], based on 9 species and 21 reactions, is taken as a benchmark to construct and validate the proposed reduced one-step scheme. For the derivation of the reaction rate parameters, calculations of steady one-dimensional (1D) planar deflagrations are performed. It is worth recalling that this configuration does not account for thermodiffusive effects. One-dimensional flame calculations are performed using the numerical solver Cantera [37]. Results obtained with the derived scheme are also compared with additional 1D flame calculations performed with the Konnov mechanism [38], accounting for 15 species and 75 reactions and the H2_NOX_15_94_TC scheme [39], based on 15 species and 47 reactions, and derived from the CRECK mechanism [40], as well as with experimental measurements, when available in the literature. The calculations are performed on a range of equivalence ratios between 0.4 and 6.0, and for system pressures between 1 and 30 atm, with the corresponding unburned gas temperatures ranging between 300 and 800 K, i.e., operating ranges typical of air-breathing combustion systems such as gas turbines, boilers, furnaces, and internal combustion engines. Compared to other reduced global mechanisms available in the literature and derived with similar best-fitting approaches, the scheme proposed in this study has a wider range of validity. Moreover, despite being optimized for the aforementioned ranges of parameters, its implementation with other operating conditions is still possible, leaving room for its further extension to other applications of interest.

2.1. Fundamental considerations in the definition of the one-step global scheme

The single overall reaction for hydrogen oxidation can be expressed as:

$$2\,H_2 + O_2 \longrightarrow 2\,H_2O. \tag{1}$$

This subtends the assumption of complete combustion, since minor species are not considered. For hydrocarbons, this hypothesis is well in agreement with chemical equilibrium, which strongly favors the conversion of the fuel molecule. However, for hydrogen fuel, the equilibrium solution involving the four main species (i.e., H_2, O_2, H_2O, and N_2) does not lead to complete fuel oxidation, as it can be observed from the adiabatic temperature calculations at variable equivalence ratios shown in Fig. 1, resulting from premixed flame simulations at $p = 1$ atm and $T_u = 300$ K (reference temperature and pressure, or RTP). The complete combustion process, which intrinsically behaves like a

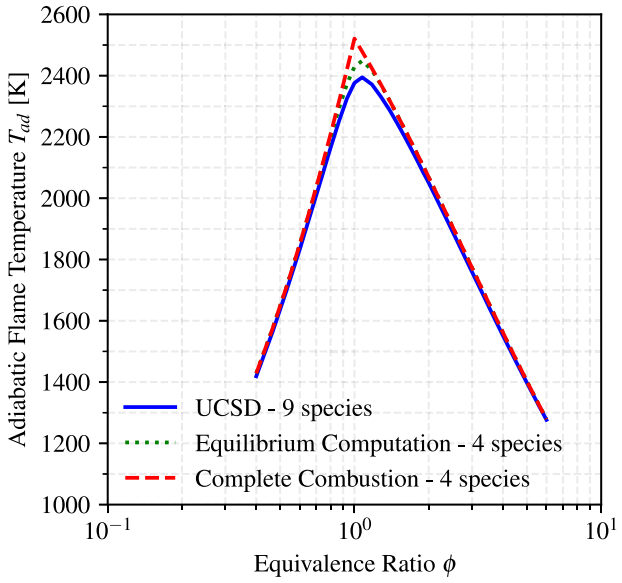

Fig. 1. Adiabatic flame temperature of hydrogen-air flames as a function of equivalence ratio at RTP. Comparison between 0D equilibrium and complete combustion calculations involving 4 species (H_2, O_2, H_2O, and N_2), and reference 1D flame calculations based on the UCSD mechanism with 9 species.

single irreversible step and is based on mixture enthalpy conservation for constant pressure processes, overestimates the adiabatic flame temperature, especially in the near-stoichiometry region, and misplaces the peak value. Conversely, the equilibrium computation, consistent with a single reversible step, provides a much more realistic solution, resulting in a better prediction of flame structure for near-stoichiometry compositions.

Based on these considerations, in the present study two different mechanisms are studied beforehand: one based on the irreversible step defined in Eq. (1), denominated 1S_IRR_H2AIR_FGS, and a second one, named 1S_REV_H2AIR_FGS, based on the following global reversible reaction:

$$2\,H_2 + O_2 \rightleftharpoons 2\,H_2O. \tag{2}$$

In both cases, the burning flux is solely dependent on the reaction rate parameters of the forward reaction constant k_f, namely the pre-exponential factor A_f, the temperature exponent β, and the activation energy $E_{a,f}$, other than the reaction order n. Hence, given a solution of the burning flux m^0 (or, equivalently, of the laminar flame speed S_L^0) obtained with detailed chemistry, a set of reaction rate parameters can be found for which the one-step chemistry model most closely follows the detailed one.

In this work, these parameters are derived for a one-step hydrogen-air scheme, following a "best-fit" approach with respect to the laminar burning flux profile m^0 obtained from the San Diego mechanism.

In principle, the fresh gas mixture conditions have an impact on the flame structure, and, consequently, the three parameters should be defined as a function of equivalence ratio, pressure, and temperature. At first, we focus on the dependency on equivalence ratio by considering a combustion process at reference temperature and pressure. Hence, the forward reaction rate coefficient can be expressed following a modified Arrhenius equation:

$$k_f(\phi) = A_f(\phi)T^{\beta(\phi)} \exp\left[-E_{a,f}(\phi)/(RT)\right]. \tag{3}$$

Aiming for a simple implementation of the reduced scheme in numerical codes, the impact of the equivalence ratio ϕ on the temperature exponent β, as well as on the activation energy $E_{a,f}$, is made implicit, by discharging the whole dependency on equivalence ratio over the Pre-Exponential Factor A, as proposed by the Pre-Exponential Adjustment (PEA) method [34]. Consequently, the forward reaction rate constant is expressed as follows:

$$k_f(\phi) = B_f(\phi)T^{\beta^*} \exp\left[-E^*_{a,f}/(RT)\right], \tag{4}$$

with

$$B_f(\phi) = A_f(\phi)T^{\beta(\phi)-\beta^*} \exp\left[-\left(E_{a,f}(\phi) - E^*_{a,f}\right)/(RT)\right], \tag{5}$$

where the superscript $*$ denotes the value computed for $\phi = 1$. Analogously, the reaction rate constant for the backward reaction in the reversible mechanism is defined as

$$k_b(\phi) = B_b(\phi) \exp\left[-E^*_{a,b}/(RT)\right], \tag{6}$$

with

$$B_b(\phi) = A_b(\phi) \exp\left[-\left(E_{a,b}(\phi) - E^*_{a,b}\right)/(RT)\right], \tag{7}$$

where the temperature exponent is, in this case, equal to zero, while the Pre-Exponential Factor and the activation energy are estimated from the values determined for the forward reaction, exploiting equilibrium considerations.

As observed in [41], the equivalence ratio ϕ affects also the overall reaction order n, as well as the ratio between the orders of fuel and oxidizer, driving the species concentrations in the overall reaction rates:

$$\omega_f = B_f(\phi)T^{\beta^*} \exp\left[-E^*_{a,f}/(RT)\right] [H_2]^{n_{H_2}} [O_2]^{n_{O_2}}, \tag{8a}$$

and

$$\omega_b = B_b(\phi) \exp\left[-E^*_{a,b}/(RT)\right] [H_2O]^{n_{H_2O}}. \tag{8b}$$

Coherently with the previous considerations, the temperature exponent and overall reaction orders are evaluated at stoichiometry (β^*, $n^*_{H_2}$ and $n^*_{O_2}$ for the forward step, and $n^*_{H_2O}$ for the backward step in the reversible mechanism) and estimated from n^*.

2.2. Estimation of the reaction order n and the temperature exponent β

Based on heat and mass balance considerations, Egolfopoulos and Law [42] proposed the concept of overall reaction order, defined as

$$n = 2\frac{\partial\left[\ln\left(m^0\right)\right]}{\partial[\ln(p)]}\bigg|_{T_{ad}}. \tag{9}$$

From a numerical point of view, the derivative in Eq. (9) can be approximated as

$$n \approx 2\frac{\ln\left[m^0(p_1)\right] - \ln\left[m^0(p_2)\right]}{\ln(p_1) - \ln(p_2)}\bigg|_{T_{ad}}, \tag{10}$$

where $p_1 = p - \Delta p$ and $p_2 = p + \Delta p$, and Δp is a small perturbation of the initial value of pressure p, which keeps the variation of adiabatic flame temperature negligible. Variations in unburned gas temperature and pressure affect the flame properties (i.e., the burning flux and flame speed) in opposite ways [42]. This could lead, in principle, to separately analyze the two influences, for example by means of power law correlations describing the laminar flame speed dependency on pressure and temperature [43]. Although numerics and experiments converge on such correlations for hydrocarbons, the same relations are not as accurate for hydrogen-air flames, and it can be deduced that the temperature and pressure exponents cannot be treated as constant for hydrogen flames, even in first approximation [44]. Moreover, from an engineering point of view, there is no actual meaning in separating temperature and pressure effects since, in real systems (e.g., industrial or aircraft gas turbines, and internal combustion engines), no compression occurs without a concurrent increase in temperature. Consequently, in the following, the influence of the initial thermodynamic state is assessed by considering only the system pressure as independent variable,

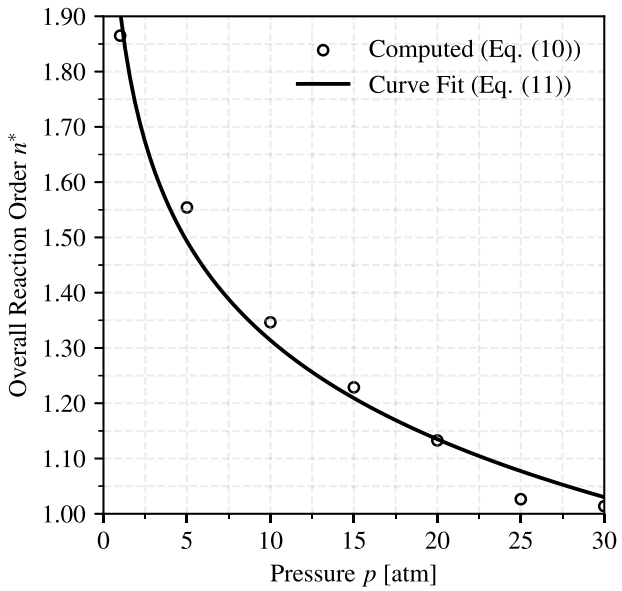

Fig. 2. Pressure dependence of overall reaction order n^* for hydrogen-air flames at $\phi = 1$. Comparison between computed values (Eq. (10)) and fitting curve (Eq. (11)).

while the unburned gas temperature is obtained, in first approximation, with the isentropic relation $T_u = T_u^0 \left(p/p^0\right)^{(k-1)/k}$, where $T_u^0 = 300$ K, $p^0 = 1$ atm, and $k = 1.4$.

Fig. 2 shows the pressure dependence of the overall reaction order, evaluated according to Eq. (10), as well as the values obtained from the logarithmic fit law

$$n^* = 1.909 - 0.2583 \ln\left(p/p^0\right). \tag{11}$$

As previously anticipated, the so-determined overall reaction order is used to estimate the temperature exponent β^*. In the proposed global mechanism, no radical formation (or consumption) is considered, and the preheat and reaction zones in the flame front are expected to be sensibly reduced. Moreover, Fig. 1 illustrates that the predicted adiabatic flame temperature is higher than in the case of detailed kinetics. Consequently, a negative exponent is required, to compensate for the overestimation of temperature and locally reduce the reaction rate in correspondence of the flame front. Based on these considerations, and recalling that, in this study, variations in unburned gas temperature and system pressure are interdependent, a value of β^* equal to $n^*/2 - 1$ is adopted. Concerning the reaction orders of the single species, $n^*_{H_2}$ and $n^*_{O_2}$ are determined from n^* by considering that $n^*_{H_2} + n^*_{O_2} = n^*$, and $n^*_{H_2}/n^*_{O_2} = \nu_{H_2}/\nu_{O_2} = 2$. By keeping the parallelism between stoichiometric coefficients and reaction orders, the value of $n^*_{H_2O}$ for the backward reaction is hence assessed as equal to $n^*_{H_2}$ of the forward step.

2.3. Estimation of the overall activation energy E_a

With similar arguments as for the overall reaction order, an overall activation energy was defined in [42] as

$$E_a = -2R \left.\frac{\partial\left[\ln\left(m^0\right)\right]}{\partial\left(1/T_{ad}\right)}\right|_p. \tag{12}$$

Based on the approach proposed in [41], to change the adiabatic flame temperature, and thereby the laminar burning flux, at constant pressure, unburned gas temperature and composition, the concentration of inert species (N_2) is varied by a small perturbation $\Delta\chi_{N_2}$. Consequently, Eq. (12) can be rewritten as

$$E_a \approx -2R \left.\frac{\ln\left[m^0\left(\chi_{N_2,1}\right)\right] - \ln\left[m^0\left(\chi_{N_2,2}\right)\right]}{1/T_{ad}\left(\chi_{N_2,1}\right) - 1/T_{ad}\left(\chi_{N_2,2}\right)}\right|_p, \tag{13}$$

where $\chi_{N_2,1} = \chi_{N_2} - \Delta\chi_{N_2}$ and $\chi_{N_2,2} = \chi_{N_2} + \Delta\chi_{N_2}$. The activation energy of the forward reaction $E^*_{a,f}$ is therefore obtained by applying this methodology for $\phi = 1$. A logarithmic dependence of this quantity with respect to pressure is found:

$$E^*_{a,f}\ [\text{kcal/mol}] = 4.893 \ln\left(p/p^0\right) + 32.97. \tag{14}$$

Fig. 3 illustrates the comparison between the values computed in agreement with Eq. (13), and the fitting function of Eq. (14).

For the backward reaction, the enthalpy of reaction evaluated at $\phi = 1$ can be used to determine the corresponding activation energy $E^*_{a,b}$:

$$E^*_{a,b} = E^*_{a,f} - \Delta H_R\big|_{\phi=1}, \tag{15}$$

where, for an exothermic process as combustion, $\Delta H_R < 0$, leading to $E_{a,b} > E_{a,f}$. A second logarithmic law, analogous to Eq. (14) and illustrated in Fig. 3, can be derived:

$$E^*_{a,b}\ [\text{kcal/mol}] = 4.825 \ln\left(p/p^0\right) + 53.05. \tag{16}$$

2.4. Definition of the Pre-Exponential Adjustment laws

Following the work by Franzelli et al. [34], two Pre-Exponential Adjustment laws are defined, one for the irreversible mechanism and the other for the reversible scheme. Both laws are based on the product of three terms:

$$B_f(\phi, p) = B^*_f(p)\ f(\phi)\big|_{p=p^0}\ g(\phi, p). \tag{17}$$

These terms are constructed by performing calculations of steady one-dimensional planar deflagrations, and by defining the best-fitting function matching the burning flux computed with the detailed San Diego mechanism. The best-fitting process is performed by minimizing the objective function, defined as the absolute value of the relative percentage error ε between the laminar burning flux m^0, computed with the reduced scheme, and the reference solution m^0_{ref} evaluated with the reference detailed mechanism:

$$\varepsilon(B(\phi,p),\phi,p)\ [\%] = 100 \frac{\left|m^0(B(\phi,p),\phi,p) - m^0_{ref}(\phi,p)\right|}{m^0_{ref}(\phi,p)}. \tag{18}$$

For a laminar planar unstretched flame, the laminar burning flux can be evaluated as

$$m^0 = \rho_u S^0_L = \rho_u S_c, \tag{19}$$

with S_c being the consumption speed, defined as

$$S_c = -\frac{1}{\rho_u\left(Y^u_F - Y^b_F\right)} \int_{-\infty}^{+\infty} \dot{\omega}_F d\mathbf{n}, \tag{20}$$

where $\dot{\omega}_F$ is the fuel consumption rate, namely the net production rate of fuel with opposite sign, and $\mathbf{n}$ is the local normal vector to the flame front, directed toward the fresh gas [43]. The target values of $B(\phi, p)$ (i.e., those minimizing ε) are therefore found by numerically solving the equation $\varepsilon = 0$ in all the range of operating conditions of interest. Subsequently, the expressions for the three functions in Eq. (17) are defined by determining, for each of them, the curve most similar to the target distribution and estimating its coefficients. A flowchart illustrating the process can be found in Fig. S3 of the Supplementary material.

Since the reaction constant of the backward reaction is three orders of magnitude lower than the forward one (see Fig. 5), the step $2\,H_2O \longrightarrow 2\,H_2 + O_2$ affects only in a limited way the burning flux (or, equivalently, the burning rate). Therefore, the same construction of the PEA law can be retained for the irreversible and the reversible global mechanisms, and the latter can be seen as an extension, or improvement, of the first, rather than a different reaction scheme.

Consequently, the Pre-Exponential Factor for the forward step can be modeled in the same way both for the irreversible and reversible

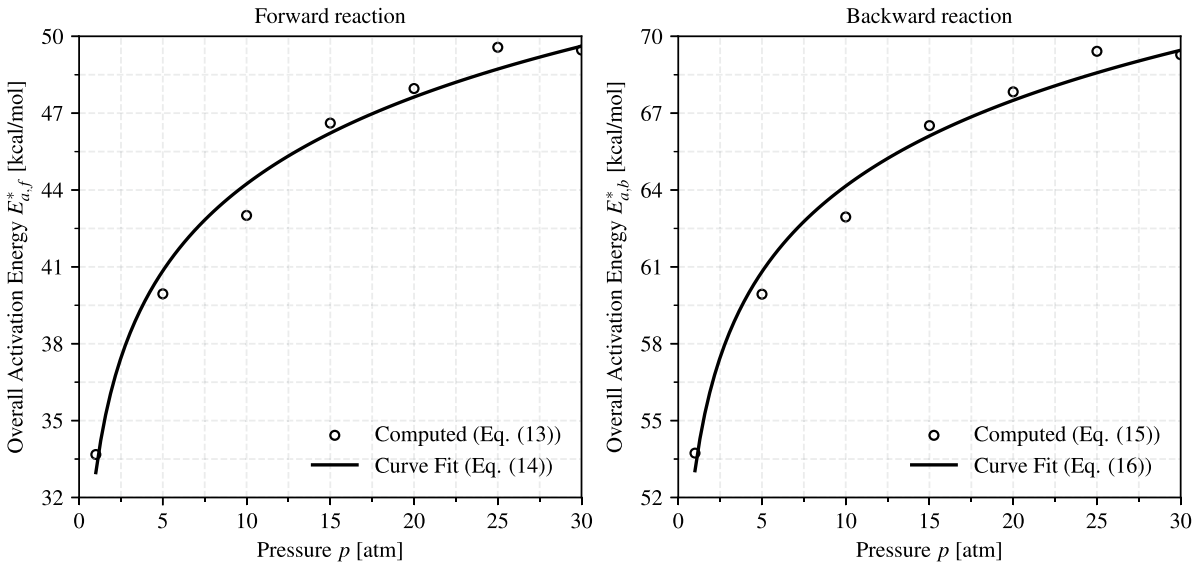

Fig. 3. Pressure dependence of overall activation energies $E^*_{a,f}$ (left) and $E^*_{a,b}$ (right) for hydrogen-air flames at $\phi = 1$. Comparison between computed values (Eqs. (13) and (15)) and fitting curves (Eqs. (14) and (16)).

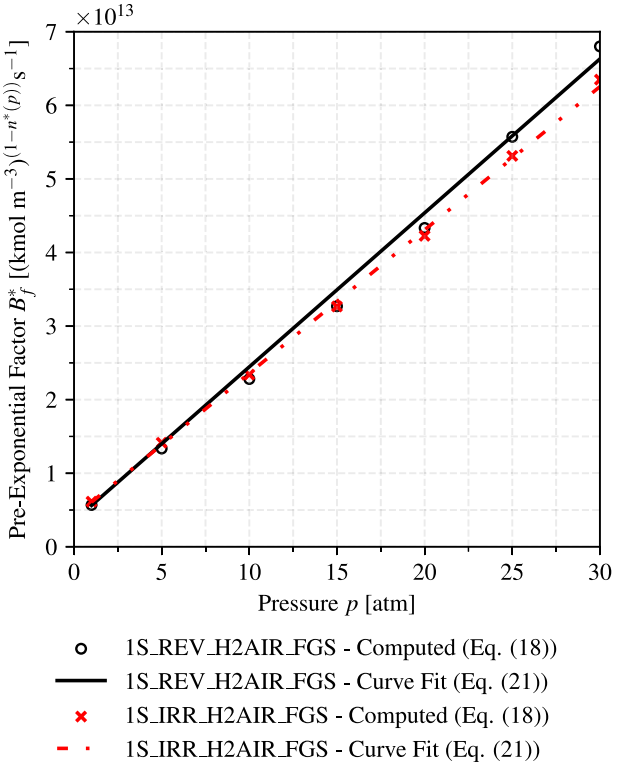

Fig. 4. Pressure dependence of the Pre-Exponential Factors of the irreversible (in red) and reversible (in black) schemes for hydrogen-air flames at $\phi = 1$. Comparison between computed values (Eq. (18)) and fitting curves (Eq. (21)). (For interpretation of the references to color in this figure legend, the reader is referred to the web version of this article.)

steps. In the following, the derivation of the three terms in Eq. (17) is presented for the two reduced schemes.

The term $B^*_f(p)$ corresponds to the Pre-Exponential Factor matching the laminar burning flux of detailed chemistry at stoichiometry. As shown in Fig. 4, a linear dependence between this coefficient and pressure is observed:

$$B^*_f(p)\left[\left(\text{kmol m}^{-3}\right)^{(1-n^*(p))}\text{s}^{-1}\right] = \left(m\frac{p}{p^0}+q\right)\times 10^{12}, \tag{21}$$

where m and q are equal, respectively, to 1.947 and 4.125 for the irreversible mechanism, and to 2.092 and 3.535 for the reversible one. It is worth noticing that the difference between the values obtained from the two expressions for the irreversible and reversible mechanisms is quite negligible.

Table 1
Coefficients for the corrective function $f(\phi)|_{p=p^0}$.

Mechanism	ψ_0	ψ_1	ψ_2	ψ_3	ψ_4	φ_0	φ_1
1S_IRR_H2AIR_FGS	0.6917	1.856	2.693	0.8530	0.1710	0.3635	3.910
1S_REV_H2AIR_FGS	0.7514	1.987	36.50	3.014	0.1818	0.3635	3.953

The corrective function $f(\phi)|_{p=p^0}$ takes into account the variability due to the different initial fuel concentration in the reference configuration, namely for $p = p^0 = 1$ atm. This function is obtained by solving Eq. (18) at RTP for 40 different values of equivalence ratio in the interval [0.4; 6.0]. It assumes the following form, with the values of the coefficients reported in Table 1:

$$f(\phi)|_{p=p^0} = \psi_0 + \psi_1 \exp\left[-\psi_2\left(\frac{\phi-\varphi_0}{\psi_3}\right)^2\right] + \psi_4 \tanh\left(\phi-\varphi_1\right). \tag{22}$$

The function $g(\phi, p)$ accounts for the increase of pressure (hence, of unburned gas temperature) at different equivalence ratios, necessary to capture the different behavior noted between lean and rich flames. Indeed, coherently with the analysis of pressure effects performed in [36], when the value of burning flux is imposed to match detailed chemistry, lean flames show a decreasing trend in the value of the Pre-Exponential Factor, while rich flames behave in the opposite way. This results in the following expression[1]:

$$g(\phi,p) = \left[\xi_0 + \xi_1 \tanh\left(\phi-\varphi_2\right)\right]^{\left[\xi_2 \ln\left(p/p^0\right)\right]}, \tag{23}$$

[1] With this mathematical expression, $g(\phi, p)$ is defined for $[\xi_0 + \xi_1 \tanh(\phi - \varphi_2)] \geq 0$, namely for $\phi \geq 0.3108$. To avoid any error if applying the reduced scheme at $p > 1$ atm in the ultra-lean regime, outside the range of validation and optimization of the mechanism (i.e., $0.4 \leq \phi \leq 6.0$), the condition $\phi = \max(\phi, \phi_{lim})$, with $\phi_{lim} \geq 0.3108$, should be adopted for this function. In this work, $\phi_{lim} = 0.3125$ is considered.

Table 2
Coefficients for the corrective function $g(\phi, p)$.

Mechanism	ξ_0	ξ_1	ξ_2	φ_2
1S_IRR_H2AIR_FGS	6.416	6.744	0.1583	2.057
1S_REV_H2AIR_FGS	7.670	8.077	0.1377	2.138

with the coefficients' values listed in Table 2 for both the irreversible and reversible schemes. This expression is constructed to decouple the composition and pressure effects, allowing for a simple integration of such a law in numerical simulation codes.

Regarding the backward reaction of the reversible scheme, its Pre-Exponential Factor is evaluated by an explicit expression, which models equilibrium by imposing the equality between the forward and backward reaction rates:

$$B_b^*(\phi) = \frac{k_f(\phi)\left[\mathrm{H_2}\right]_{eq}^{n^*_{\mathrm{H_2}}}\left[\mathrm{O_2}\right]_{eq}^{n^*_{\mathrm{O_2}}}}{\exp\left[-E^*_{a,b}/\left(RT_{eq}\right)\right]\left[\mathrm{H_2O}\right]_{eq}^{n^*_{\mathrm{H_2O}}}} = = B_f^*(\phi)\frac{T_{eq}^{\beta^*}\exp\left[-E^*_{a,f}/\left(RT_{eq}\right)\right]\left[\mathrm{H_2}\right]_{eq}^{n^*_{\mathrm{H_2}}}\left[\mathrm{O_2}\right]_{eq}^{n^*_{\mathrm{O_2}}}}{\exp\left[-E^*_{a,b}/\left(RT_{eq}\right)\right]\left[\mathrm{H_2O}\right]_{eq}^{n^*_{\mathrm{H_2O}}}}. \quad (24)$$

The scaling factor between $B_f(\phi)$ and $B_b(\phi)$, which can be easily evaluated by zero-dimensional (0D) equilibrium calculations, is here analytically defined as:

$$h(\phi, p)\ \left[\left(\mathrm{kmol\ m^{-3}}\right)^{n^*_{\mathrm{O_2}}(p)}\right] = \frac{B_b^*(\phi)}{B_f^*(\phi)} = \frac{\varsigma_0(p)\varsigma_1^2(p)}{\left(\frac{40\phi}{40\phi+43} - \frac{1}{2}\right)^2 + \varsigma_1^2(p)}, \quad (25)$$

where the pressure-dependent coefficients ς_0 and ς_1 are modeled as follows:

$$\varsigma_0(p) = \left[0.2320\ln^2\left(p/p^0\right) + 1.392\ln\left(p/p^0\right) + 1.568\right]\times 10^{-2}, \quad (26a)$$

and

$$\varsigma_1(p) = \left[0.8336\ln^2\left(p/p^0\right) + 0.3220\ln\left(p/p^0\right) + 5.815\right]\times 10^{-2}. \quad (26b)$$

The functions $f(\phi)|_{p=p^0}$, $g(\phi, p)$ and $h(\phi, p)$ are shown in Fig. 5, where the impact of pressure on $g(\phi, p)$ and $h(\phi, p)$ is emphasized. It is worth noticing that, as previously anticipated, the maximum value of $h(\phi, p)$ is in the order of 10^{-3}, hence the influence of the backward step is negligible for many flame conditions, and mostly limited to the near-stoichiometric region, where the peak value is reached.

2.5. Correction for flame thickness

To the best of our knowledge, the impact of simplified kinetics on flame thickness has been usually neglected in the definition and validation of reduced chemistry mechanisms for combustion reported in the literature. Nevertheless, since the best-fit approach involves global flame properties such as the burning flux and the flame speed, the chemical source terms are well-described by the reduced kinetics only in an integral form. The local flame structure is not controlled, and, in particular, the mass fractions and thermal gradients, defining the "thermal" flame thickness δ_L^0 [43]

$$\delta_L^0 = \left|\frac{T_b - T_u}{\max(\nabla T)}\right|, \quad (27)$$

are not ensured. Numerical computations demonstrate that, compared to the detailed mechanism, the reduced schemes predict higher values of the adiabatic flame temperature, and of the heat release rate, leading to a steeper gradient in the profiles of species mass fractions and temperature (as will be further discussed in Fig. 8 of Section 3.1). This generates a nonphysical thinner flame, which may represent an issue from a numerical point of view in CFD simulations.

Table 3
Coefficients for the FTA function.

i	1	2	3	4	5	6
σ_i	1043	20.00	41.26	0.3670	8.060	1.148

Table 4
Parameters adopted in the transport model for the reduced scheme.

Sc_0				Pr_0	μ_0 [kg/(m s)]	T_0 [K]	α
H_2	O_2	H_2O	N_2				
0.2507	0.7732	1.168	0.9056	0.6292	8.063×10^{-5}	2645	0.6481

A correction is here proposed to properly match the flame thickness with reduced chemistry. Since the reaction rate parameters are already defined to match the flame speed and burning flux, the sole quantities on which an adjustment may be performed are the inherent properties of species: the thermodynamic quantities, namely the specific heat capacities and the enthalpies of formation, and the diffusivities. The proposed model intervenes on thermal and mass species diffusivities, adapting the methodology proposed by Butler and O'Rourke [45], which constitutes the basis of the Thickened Flame model adopted for LES calculations of reacting flows (TFLES) [43]. In particular, a multiplicative term is introduced in the expression of the Pre-Exponential Factor, which will be referred to in this work as Flame Thickness Adjustment (FTA). The FTA function is defined from the ratio between the actual flame thickness, computed with detailed chemistry, and the one deriving from the previously defined one-step scheme, and modeled as follows:

$$FTA(\phi) = \frac{\sigma_1}{1+\exp\left(-\frac{\phi+\sigma_2-\sigma_3/2}{\sigma_4}\right)}\left[1 - \frac{1}{1+\exp\left(-\frac{\phi+\sigma_2+\sigma_3/2}{\sigma_5}\right)}\right] - \sigma_6, \quad (28)$$

where the coefficients σ_i are reported in Table 3. In principle, this function should be pressure-dependent; however, this would dramatically increase the stiffness of the model, limiting the advantages of a reduced scheme in terms of computational cost. For this reason, a single function has been adapted to capture, with a single set of parameters, the behavior of the reduced kinetics in the whole range of pressures of interest. Such a compromise, however, does not introduce a significant error since the pressure-sensitivity of the thickness reduction, when passing from detailed to global chemistry, is negligible (see Fig. 8 in Section 3.1).

In agreement with [45], all diffusivities are multiplied by the FTA function, while the reaction rates, and in particular the Pre-Exponential Factors $B_f(\phi)$ and $B_b(\phi)$, are divided by it. In the transport model adopted for the reduced mechanism in this study, a simplified non-unity Lewis number approach is applied, based on constant species Schmidt and mixture Prandtl numbers, and a simple fitting power law $\mu(T) = \mu_0\left(T/T_0\right)^\alpha$ is used for the viscosity. The transport parameters are reported in Table 4, where Pr_0 and Sc_0 represent the values of the Prandtl and Schmidt numbers before applying the FTA correction.

3. Validation of the global reaction mechanism

The validity of the proposed one-step mechanism, with particular reference to the reversible one (1S_REV_H2AIR_FGS), is tested by comparing the results obtained with the global scheme for several unstretched and stretched configurations involving hydrogen-air mixtures of different compositions and thermodynamic states with experimental measurements available in the literature and calculations performed with reference reaction schemes.

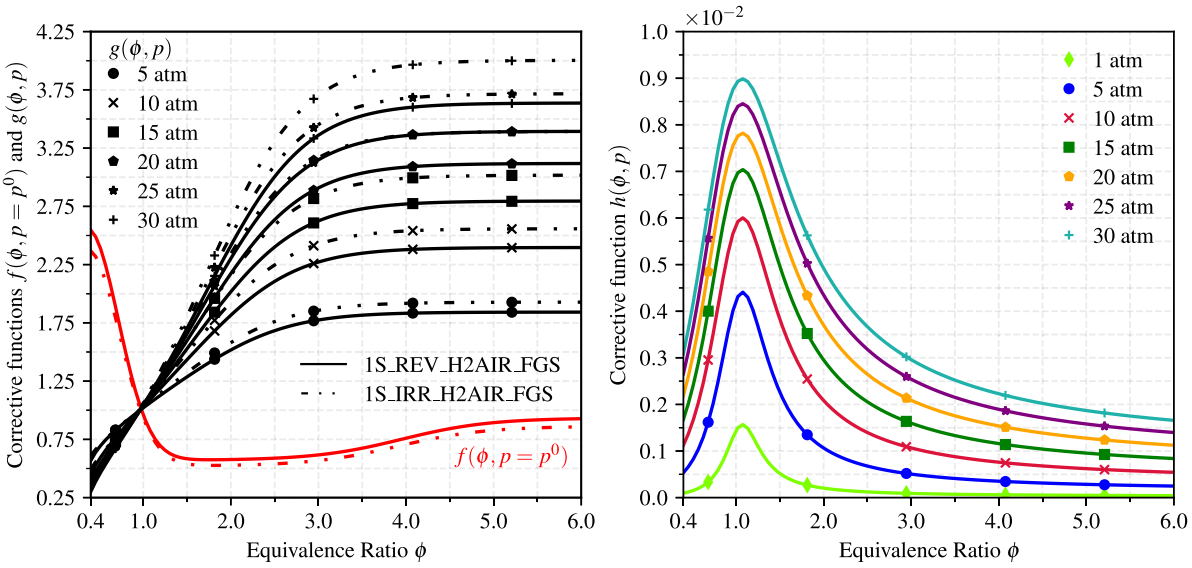

Fig. 5. Evolution, versus equivalence ratio, of the corrective functions $f(\phi)|_{p=p^0}$ (left, in red) and $g(\phi, p)$ (left, in black) for the irreversible and reversible schemes, and of the corrective function $h(\phi, p)$ (right) for the reversible scheme. (For interpretation of the references to color in this figure legend, the reader is referred to the web version of this article.)

3.1. Unstretched flames

First, freely-propagating, unstretched laminar premixed flames under various combinations of equivalence ratio, pressure and unburned gas temperature are solved in Cantera.

A domain of length equal to 5 cm is considered to be 2–3 orders of magnitude larger than flame thickness, avoiding any impact of boundaries on the flame solution. Mesh refinement criteria are adopted, so that the number of grid points for each case is in the order of 10^3.

In order to properly match experimental measurements, computations with detailed schemes are performed by adopting a multicomponent transport model [46] including thermophoresis (or Soret effect), which becomes relevant for hydrogen in low-velocity zones in the presence of temperature gradient [47]. The parameters of the global reaction scheme are optimized to fit the reference values computed in this way.

A comparison of laminar flame speeds predicted by the reduced mechanism and the reference detailed schemes at reference temperature and pressure is displayed in Fig. 6, where results deriving from experimental measurements are added as additional reference. At p = 1 atm, due to the methodology applied for the definition of the Pre-Exponential Adjustment law, a significantly good agreement can be observed between reduced and detailed chemistry in predicting S_L^0 in the whole range of validation of the reduced scheme (i.e., $0.4 \leq \phi \leq 6.0$). Since the multicomponent transport model and Soret effect are considered for reference calculations, the results in this range of equivalence ratios are also well in agreement with the reported values deriving from experimental tests taken from [48] and references therein [49–60]. A reasonable agreement with experimental data is found also for very lean mixtures (i.e., $\phi < 0.4$), as shown by the dashed red line in Fig. 6, even though this region is not considered for the definition and validation of the global reaction mechanism at higher pressures and temperatures.

Regarding the impact of pressure, Fig. 7 compares the results at elevated pressure (15 and 30 atm), with the corresponding unburned gas temperatures computed according to the isentropic law. The logarithmic exponent, introduced to take into account such effect, provides a reasonably good agreement for the whole range of pressures, in particular for lean flames. Compared to the San Diego and Konnov mechanisms, a moderate overprediction of velocity is present for rich flames, in particular for what concerns the peak value, due to the simplifications performed in the construction of the Pre-Exponential Adjustment laws to avoid too complex implicit expressions. Nevertheless, it can be observed that, for all configurations, the error remains well below the threshold of 10%.

As ultra-lean hydrogen-air flames at these pressure levels are of interest for practical applications (e.g., hydrogen-fueled gas turbines), values of laminar flame speed are computed with the reduced scheme also for very lean flames, up to ϕ = 0.25, and marked with dashed red lines in Fig. 7. A sufficiently adequate consistency can be observed between the reduced scheme and the detailed mechanisms even in this regime, despite the limit on the validity domain of the pressure-scaling function $g(\phi, p)$ discussed in Section 2.4. Nevertheless, aside from this limitation of the proposed model, care has to be put into the computation of laminar flame speed close to the lean flammability limit, due to the physicochemical nature of lean hydrogen flames. Indeed, at high pressures, these flames are particularly prone to Darrieus-Landau and thermodiffusive instabilities, which produce severe flame wrinkling, with an associated increase in burning velocity [61]. One-dimensional flame calculations do not consider flame instabilities, hence compromising the accuracy of the numerically computed values of laminar flame speed even with detailed reaction mechanisms. To account for the effect of instabilities, a correction should be therefore introduced, based on the growth rates ω_{DL}, characterizing Darrieus-Landau instabilities [62], and ω_2, characterizing thermodiffusive instabilities, arising from stability analysis [63]. For further reading on the subject and examples of applications of this approach, the reader is directed, for instance, to the work by Aspden and co-workers [64,65].

We now investigate the impact of the FTA function and of the backward reaction on the proposed scheme. In particular, Fig. 8 shows the thermal flame thickness and the adiabatic flame temperature resulting from the 1S_REV_H2AIR_FGS scheme for several equivalence ratios, including the detailed mechanisms for reference.

For the flame thickness, the values obtained by imposing $FTA \equiv 1$ are reported too, in order to assess the impact of the proposed correction. For the adiabatic flame temperature, the results obtained with the reversible scheme are compared also with those deriving from the 1S_IRR_H2AIR_FGS scheme, so that the impact of the backward reaction can be evaluated. The results are reported, for the sake of brevity, only for p = 1 atm and p = 15 atm, but similar considerations can be drawn for other pressure values (e.g., see Fig. S6 of the Supplementary material for p = 30 atm).

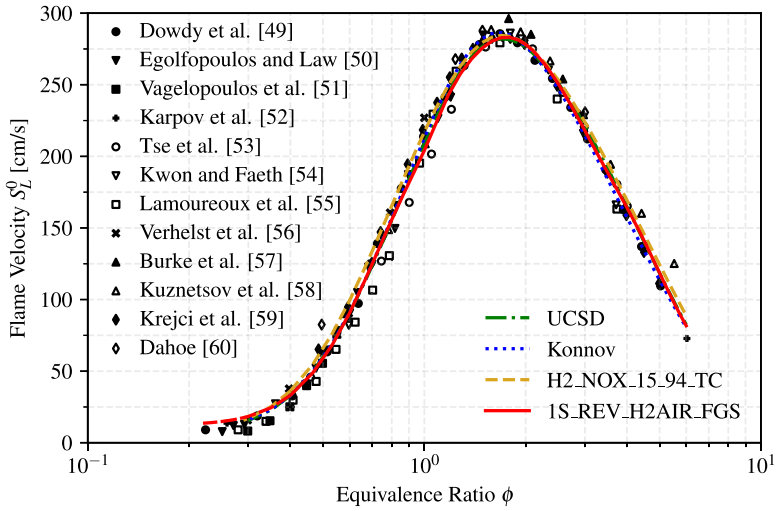

Fig. 6. Laminar flame speed of hydrogen-air planar deflagrations versus equivalence ratio at RTP. Comparison between experimental measurements (symbols) and numerical integrations with reduced 1S_REV_H2AIR_FGS scheme and reference kinetic mechanisms. Results, denoted by a dashed red line, are added for the reduced scheme in very lean mixture conditions ($\phi < 0.4$), outside its range of validation. (For interpretation of the references to color in this figure legend, the reader is referred to the web version of this article.)

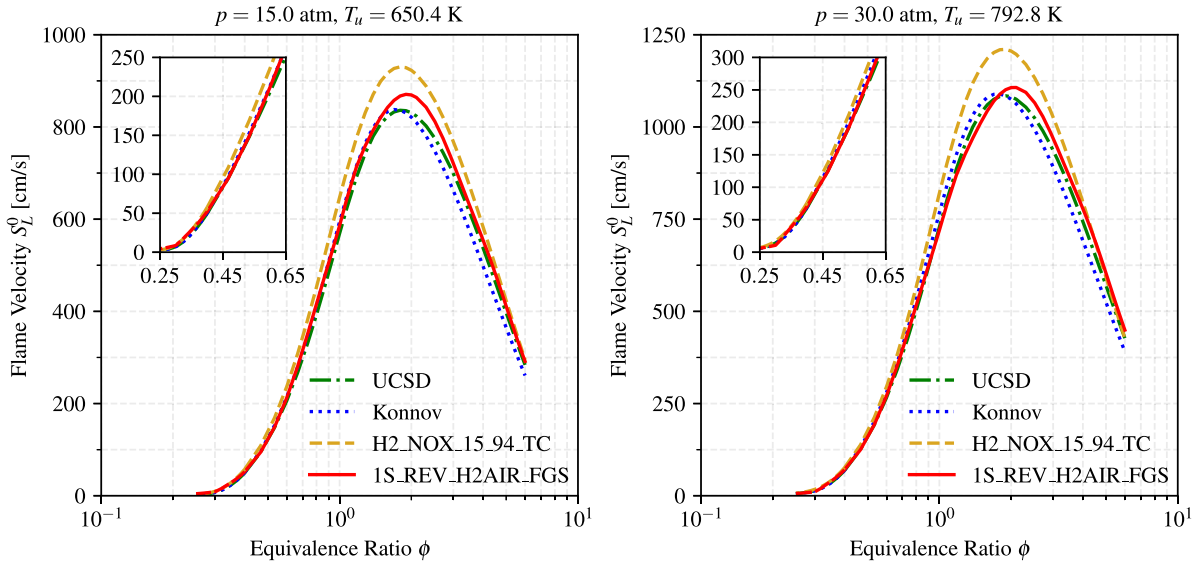

Fig. 7. Laminar flame speed of hydrogen-air planar deflagrations versus equivalence ratio at 15 atm (left) and 30 atm (right). The insets enhance the values obtained in the lean regime for $0.25 \leq \phi \leq 0.65$. Comparison between numerical integrations with reduced 1S_REV_H2AIR_FGS scheme and reference kinetic mechanisms. Results, denoted by a dashed red line, are added for the reduced scheme in very lean mixture conditions ($\phi < 0.4$), outside its range of validation. (For interpretation of the references to color in this figure legend, the reader is referred to the web version of this article.)

The thermal flame thickness, computed with the temperature profile gradient (see Eq. (27)), is the most appropriate to determine mesh resolutions in CFD calculations: the capability of a reduced scheme to predict the correct value of this quantity is beneficial for numerical stability. Fig. 8 (left) shows the importance of the FTA function introduced in the present work, which allows to adjust the temperature gradient of the reduced scheme. Since no pressure dependence has been introduced in the expression of FTA, a distinguishable, yet tolerable error is observed at RTP. Being defined on a range of pressure between 1 and 30 atm, the FTA function allows to attain the best match with reference mechanisms at $p = 15$ atm. Nevertheless, although the value of the thickness varies significantly throughout the considered pressure range, the scaling factor between the detailed chemistry and the reduced scheme proposed in this work remains almost unaffected and independent from system pressure.

For what concerns the adiabatic flame temperature, as mentioned in the previous section and shown in Fig. 8 (right), an irreversible step, based on the assumption of complete combustion, overestimates the value of the maximum adiabatic flame temperature, and incorrectly predicts the location of the peak at $\phi = 1.0$, while it should be obtained for a slightly rich mixture. On the other hand, the 1S_REV_H2AIR_FGS scheme, including the equilibrium reaction, allows to predict the flame temperature in a much more consistent way, halving to approximately 2% the maximum relative percentage error computed with respect to the San Diego scheme. It is worth noticing that the correct prediction of peak adiabatic flame temperature is significant for a potential integration of NO_x pathways in the reduced scheme, being the Zel'dovich mechanism describing nitrogen oxidation strongly dependent on temperature because of the high activation energy [66].

The impact of the backward reaction is even more evident when considering the flame structure. In particular, Fig. 9 compares the mole

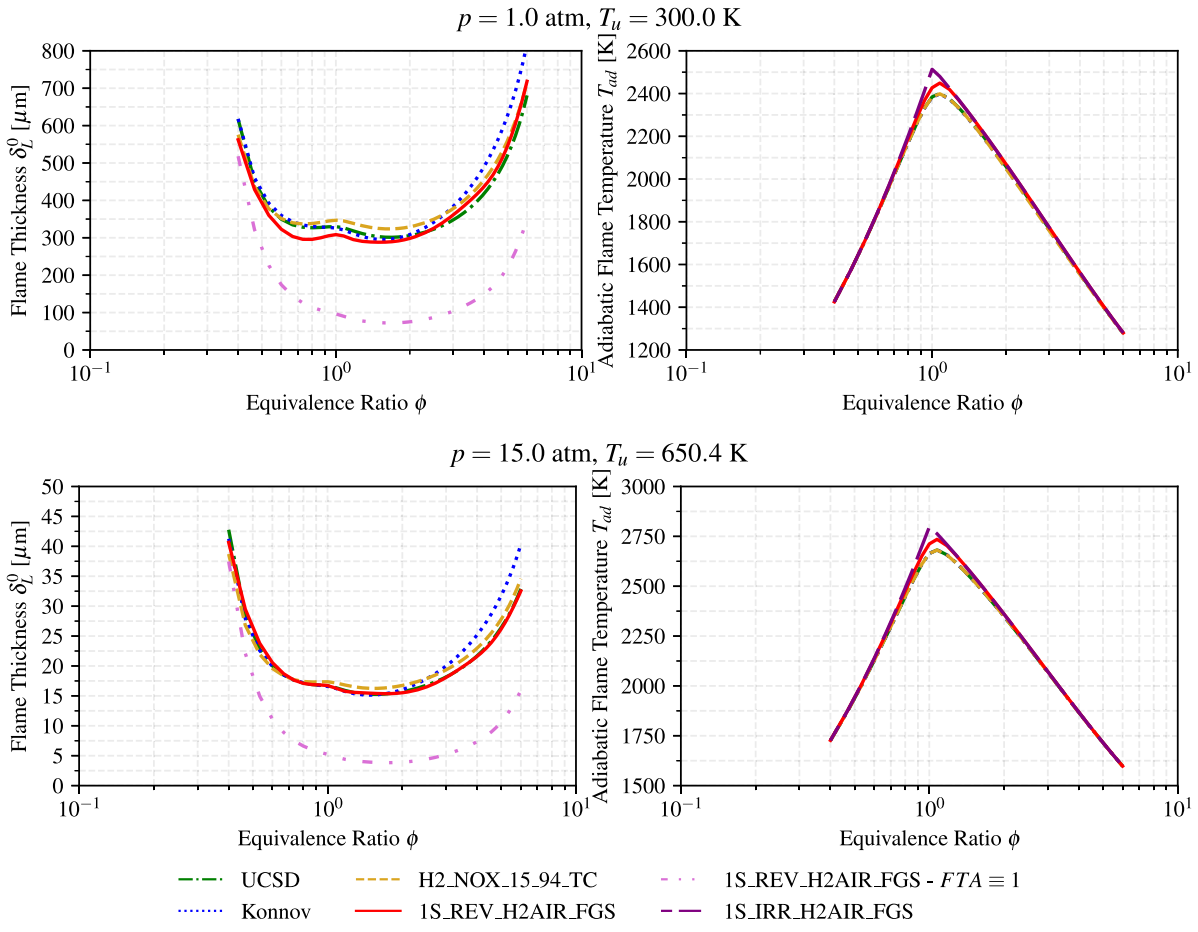

Fig. 8. Thermal flame thickness and adiabatic flame temperature of hydrogen-air planar deflagrations versus equivalence ratio at $p = 1$ atm (top) and $p = 15$ atm (bottom). Comparison between numerical integrations with reduced 1S_REV_H2AIR_FGS scheme and reference kinetic mechanisms. For the flame thickness, results for the reduced 1S_REV_H2AIR_FGS scheme without Flame Thickness Adjustment are also reported. For the adiabatic flame temperature, results for the reduced 1S_IRR_H2AIR_FGS scheme are shown.

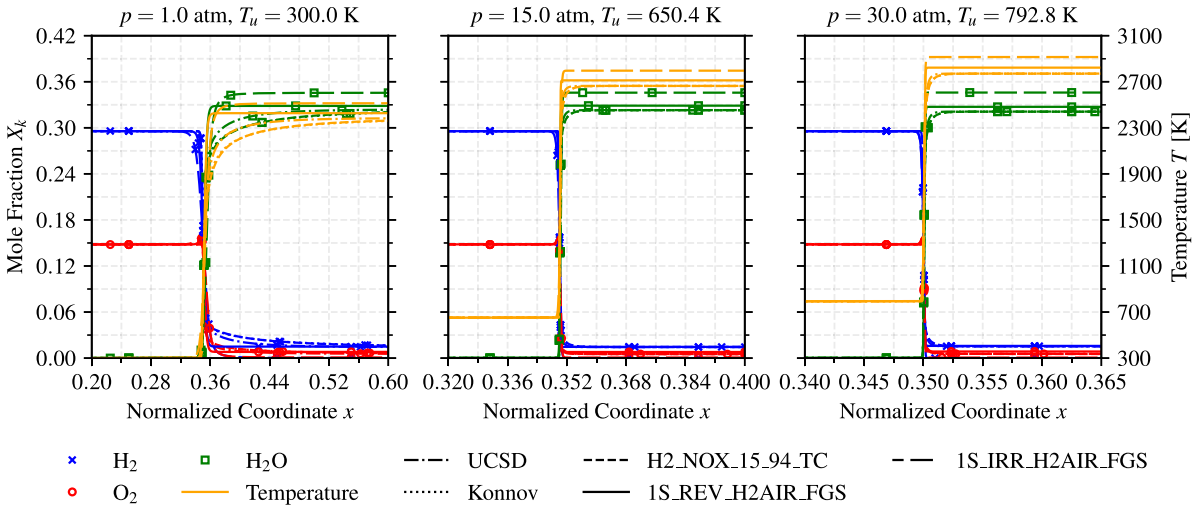

Fig. 9. Profiles of mole fractions (left axis) and temperature (right axis) across hydrogen-air planar deflagrations for $\phi = 1.0$ at 1 atm (left), 15 atm (center) and 30 atm (right). Comparison between numerical integrations with reduced 1S_REV_H2AIR_FGS and 1S_IRR_H2AIR_FGS schemes, and reference kinetic mechanisms.

fraction and temperature profiles across the flame, computed at $p = 1$ atm, $p = 15$ atm, and $p = 30$ atm with the two reduced schemes and the detailed mechanisms for stoichiometric ($\phi = 1.0$) hydrogen-air mixtures. The flame structures for the lean ($\phi = 0.4$) and rich ($\phi = 4.0$) cases are not shown here, for the sake of brevity, but they are available in Figs. S7 and S8 of the Supplementary material. Coherently with the considerations made for the adiabatic flame temperature, the most important differences between the reversible and irreversible schemes can be found at stoichiometry. Besides the already discussed difference in the prediction of flame temperature, in fact, an irreversible reaction

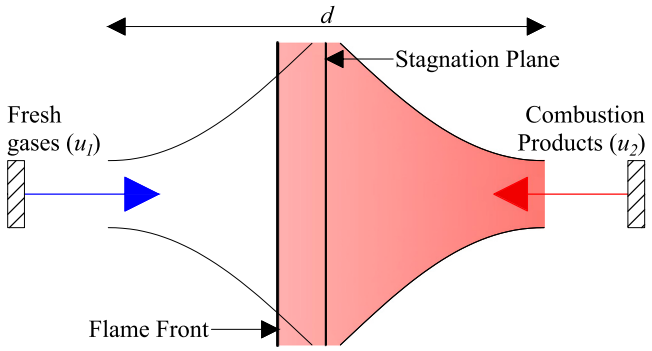

Fig. 10. Schematic representation of a counterflow premixed flame configuration. Fresh gases are injected against combustion products at equilibrium, with a steady flow.

badly predicts the final composition of the mixture, assuming that all hydrogen and oxygen are consumed, which is not physical in the actual hydrogen oxidation process. On the other hand, albeit showing steeper gradients in the flame reaction region, the 1S_REV_H2AIR_FGS matches the final composition of the mixture obtained with detailed kinetics at all pressures.

3.2. Stretched flames

The previous results have shown the capabilities of the reduced mechanism in predicting flame characteristics for unstretched steady laminar deflagrations. Nevertheless, premixed flames in practical combustion systems are subject to stretch, which modifies the internal flame structure and the resulting burning rate [20]. It is worth recalling that flame stretch is composed of two terms: strain, related to flow velocity gradient, and a term computed by the curvature of the reaction front [43]. The impact of stretch is represented by a variation of the consumption speed S_c with respect to the laminar flame speed S_L^0. In the following, the flame response to the different stretch components is assessed, by considering two flame configurations.

3.2.1. Flame response to strain

First, the performance of the proposed reversible mechanism in the prediction of strain-dependent behavior is investigated by considering a premixed counterflow flame configuration in Cantera. A steady jet of premixed fresh gases is injected in opposition to another stream composed of combustion products at the equilibrium (see Fig. 10); the value of the distance d between the jets is equal to 5 cm. In this configuration, the curvature term is zero, and the stretch coincides with the strain generated by the rapid velocity variations in the flame tangent plane [43]. The counterflow premixed flame is preferred to the premixed twin flame (where both jets are composed of fresh gases) since it is more representative of the laminar flame structure embedded in turbulent strained flames, as highlighted in [67].

Fig. 11 compares flame consumption speed, normalized with the unstretched laminar flame speed, for lean, stoichiometric, and rich flames. The strain rate is here defined as the mean strain rate $a_{mean} = (|u_1| + |u_2|)/d$, with u_1 and u_2 being the inlet velocities of jets. The reduced scheme correctly reproduces the behavior of detailed schemes for the lean ($\phi = 0.4$) and rich ($\phi = 4.0$) flames, while some differences are found for the stoichiometric case. For further analyses in this sense, the flame structures at different strain levels are provided in Figs. S9, S10 and S11 of the Supplementary material. Focusing on the $\phi = 1$ case, it is noted that the reduced scheme predicts an increasing value of speed (i.e., a negative Markstein length), while reference calculations indicate a slightly decreasing trend (i.e., a slightly positive Markstein length). The sign of the Markstein length is, according to theory, related to the value of Lewis number, with $Le > 1$ corresponding to a positive Markstein length, while the opposite occurs for $Le < 1$ [43]. A modification of the transport parameters, and in particular of the species' Lewis numbers, could therefore allow to better predict the strain-dependent behavior at stoichiometry, as it has been done by Franzelli et al. [68] for a reduced scheme describing methane-air combustion. This modification, still based on constant Lewis numbers, is not introduced here since it would induce major differences in the prediction of stretch response in the lean regime, which is of the greatest interest for hydrogen-air flames. Nevertheless, a modification of the FTA function, taking into account a dynamic variation of the Lewis numbers, could be introduced in future work to further extend the validity of the reduced mechanism; a similar approach is implemented in [69] to generalize the TFLES model to stretched flames.

3.2.2. Flame response to curvature

The reversible global reaction mechanism is here applied to a two-dimensional (2D) cylindrical expanding flame. In this configuration, the laminar flame is subjected to pure curvature, namely the strain component is null and flame stretch is given by $\kappa = \frac{1}{r}\frac{d}{dt}r(t)$, where r is the radial position of the flame front. Three different fresh gas mixture conditions are considered: a lean mixture ($\phi = 0.4$), a stoichiometric one ($\phi = 1.0$), and a rich one ($\phi = 4.0$), for reference temperature and pressure.

Direct Numerical Simulations (DNS) are carried out with the Navier–Stokes compressible DNS/LES solver AVBP (www.cerfacs.fr/avbp7x), an explicit massively-parallel code solving the conservation of mass, momentum, energy and species equations. A second-order accurate in space and time Lax–Wendroff finite-volume scheme is adopted for the discretization of convective terms [70], and a second-order finite-element Galerkin scheme is implemented for diffusion terms [71]. Domains are discretized on unstructured grids of triangular elements, with a grid resolution of $\Delta x = 25$ μm, corresponding to approximately 10 points in the flame front of the stoichiometric flame, which is the thinnest of all cases considered (see Fig. 8). The time step is determined by adopting $CFL = 0.7$ for the Courant–Friedrichs–Lewy condition, and the Fourier number Fo is set to 0.1. Outlet boundary conditions are treated with the Navier–Stokes Characteristic Boundary Conditions (NSCBC) [72,73]. The mixture is ignited using the Energy Deposition (ED) model [74]. As remarked in Section 2.5, for the reduced mechanism a simplified non-unity Lewis number transport model is adopted, based on constant mixture Prandtl Pr and species Schmidt Sc_k numbers. An analogous model is retained for CFD simulations with the San Diego scheme. For both reaction mechanisms, the values of Pr and Sc_k have been tuned to match the laminar flame speed computed in Cantera with detailed transport properties (i.e., multicomponent transport model with thermophoresis) in the operating conditions of interest.

The computational domain (see Fig. 12) is defined by a circle of radius 30 mm, at the center of which the flame is initialized. By exploiting symmetry arguments, only a quarter-circle is considered in the simulations, so that overall computational cost is reduced.

The impact of the simplified chemistry description is assessed by comparing the results obtained with the flame solutions computed using the San Diego mechanism under the same operating conditions. An aspect of interest is represented by the structure and geometry of the flame fronts. In fact, laminar premixed flames are subject to intrinsic cellular instabilities, both hydrodynamic and thermodiffusive. The hydrodynamic instability mechanism derives from the sudden density variation across the flame front and appears in all flames. The thermodiffusive instability mechanism, instead, is triggered by low fuel Lewis number values, inducing strong differential diffusion effects within the flame front; such a mechanism is characteristic of lean hydrogen flames, for which $Le < 1$ [75,76]. In cylindrical expanding flames, the positive flame stretch has a stabilizing effect on intrinsic cellular instabilities. Moreover, the tendency to form hydrodynamic and thermodiffusive instabilities can be delayed for these flames, since,

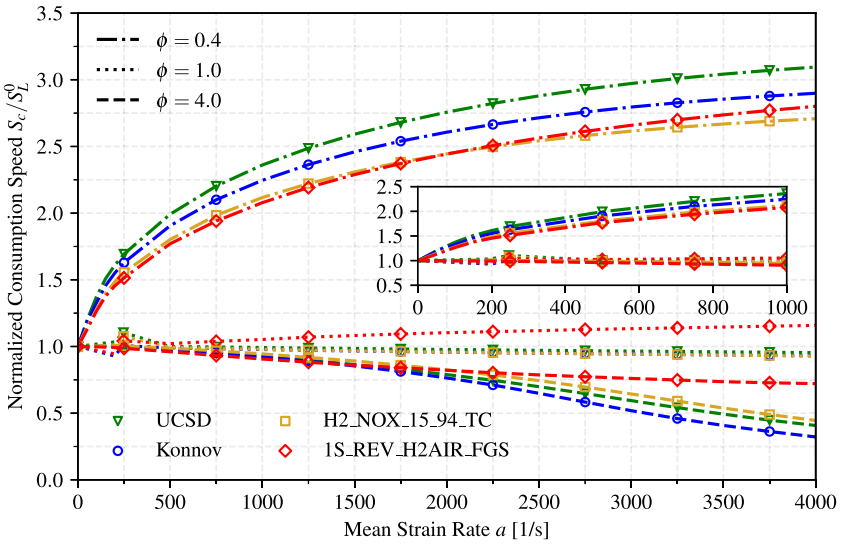

Fig. 11. Normalized consumption speed versus mean strain rate for lean (ϕ = 0.4), stoichiometric (ϕ = 1.0) and rich (ϕ = 4.0) counterflow premixed flames at RTP. The inset enhances the values calculated in the low-strain regime. Comparison between numerical integrations with reduced 1S_REV_H2AIR_FGS scheme and reference kinetic mechanisms.

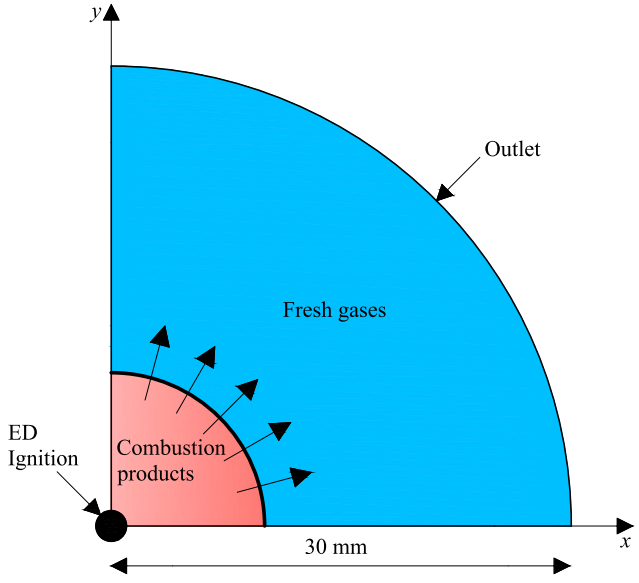

Fig. 12. Schematic representation of the computational domain adopted for the 2D cylindrical expanding flame. The flame is initialized in $x = 0$, $y = 0$ and propagates in a quarter-circle-shaped domain.

upon ignition, the flame kernel is small and the positive stretch is strong enough to suppress cell development. As a result, the flame becomes unstable only after a critical kernel size is reached, which is smaller for lower Lewis numbers [75,77]. In Fig. 13, the flame fronts derived from the numerical simulations with reduced and detailed mechanisms are compared at the same flame radius for the lean case. Coherently with the methodology proposed in [78], the flame front is here identified by considering an iso-surface of the progress variable c = 0.5, where $c = Y_{H_2O}/Y_{H_2O}^{Eq}$, and $Y_{H_2O}^{Eq}$ is the mass fraction of water in the equilibrium products for each mixture composition. Both mechanisms predict visible hydrodynamic instabilities in the flame front for the lean case (ϕ = 0.4), for which the density ratio of burned and fresh gases is higher, as well as the onset of thermodiffusive ones, which are here delayed due to the aforementioned stretch effect. For ϕ = 1.0 and ϕ = 4.0 cases, both mechanisms agree in predicting no instabilities on the flame front within the simulated physical time, as it is shown in Figs. S12 and S13 of the Supplementary material.

The validity of the reduced scheme is further assessed by considering the stretch-dependent behavior. In particular, the consumption speeds predicted at different radii by the global reaction mechanism are compared with the values given by the San Diego scheme. For this geometry, the consumption speed is evaluated by measuring the flame surface A_f and integrating the rate of reactant consumption through the entire surface Σ [79]:

$$S_c = -\frac{1}{A_f \rho_u \left(Y_F^u - Y_F^b\right)} \int_\Sigma \dot{\omega}_F d\Sigma. \tag{29}$$

The flame surface A_f, for this 2D case, is given by the circumference of radius r, namely the mean radius of the flame front. This is determined from the area A_b of the burnt gas region, identified by the condition $c \geq 0.5$, as $\sqrt{A_b/\pi}$ [78].

Fig. 14 displays the consumption speed, normalized by the unstretched laminar flame speed computed for the same mixture conditions by the CFD code, as a function of the mean flame radius for the three different mixtures. As highlighted in [80], the ignition affects the early-stage flame propagation; this is here evident from the spike in the value of speed observed for all cases. After this initial phase, a quite good agreement can be observed between the two reaction schemes in the prediction of the consumption speed for the lean and rich mixtures, with a maximum error lower than 5%, as it is shown in the inset; larger differences are found for the stoichiometric case. These results are coherent with those previously shown in Fig. 11 for the 1D counterflow premixed flame, sustaining the consistency of the proposed model. Interestingly, for larger radii (i.e., lower values of stretch), with both mechanisms the consumption speed for the lean mixture converges to a value higher than the laminar flame speed. This is explained by the fact that, for lean hydrogen flames, instabilities, as those shown in Fig. 13, have an impact on flame propagation velocity, since the total reaction rate increases as the product $I_0\Theta_0$, where $I_0 = S_c/S_L^0$ is the stretch-induced increase of consumption speed [81] (see Fig. 11), while Θ_0 is the ratio between the increased flame surface, due to the formation of cell structures on the wrinkled flame front, and the reference flame surface [82].

Finally, the reduction in computational costs, due to the simplifications in the kinetics description, is considered. Table 5 compares the maximum computed time step, derived from the imposed values for the Courant–Friedrichs–Lewy condition and the Fourier number, and the iterations per second resulting from the calculations performed with the reduced 1S_REV_H2AIR_FGS scheme and the reference San Diego

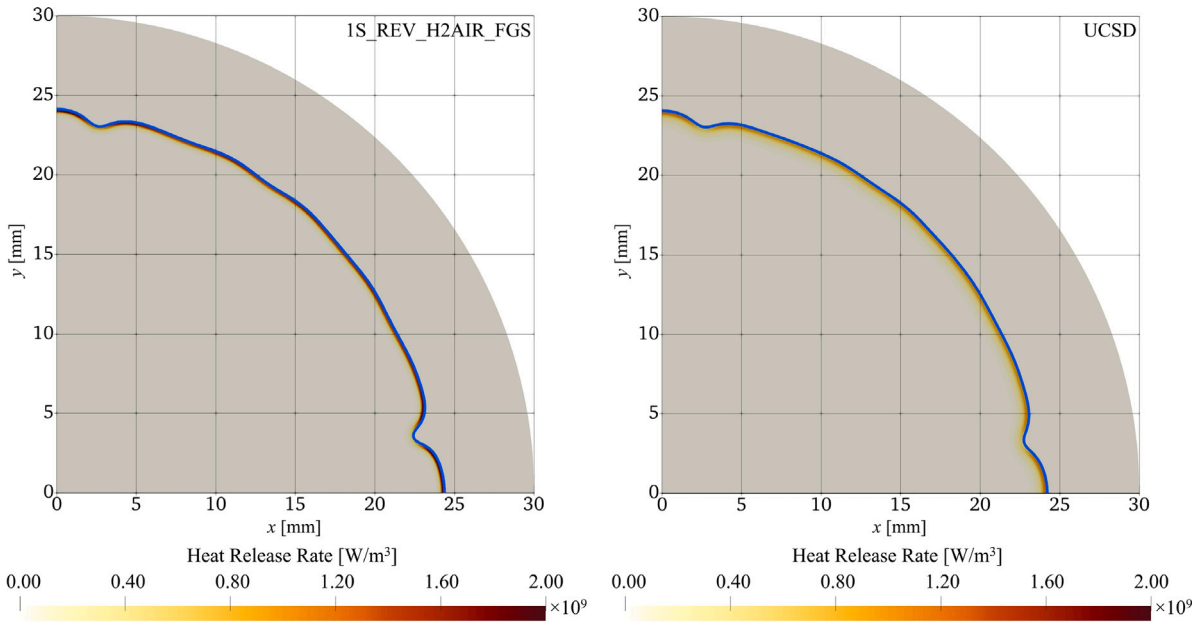

Fig. 13. Flame front of the lean 2D cylindrical expanding flame ($\phi = 0.4$) for $r = 24$ mm, identified by the iso-surface of the progress variable $c = 0.5$ (blue line), and superimposed on the Heat Release Rate field. Comparison between CFD simulations performed with reduced 1S_REV_H2AIR_FGS scheme (left) and reference UCSD mechanism (right). (For interpretation of the references to color in this figure legend, the reader is referred to the web version of this article.)

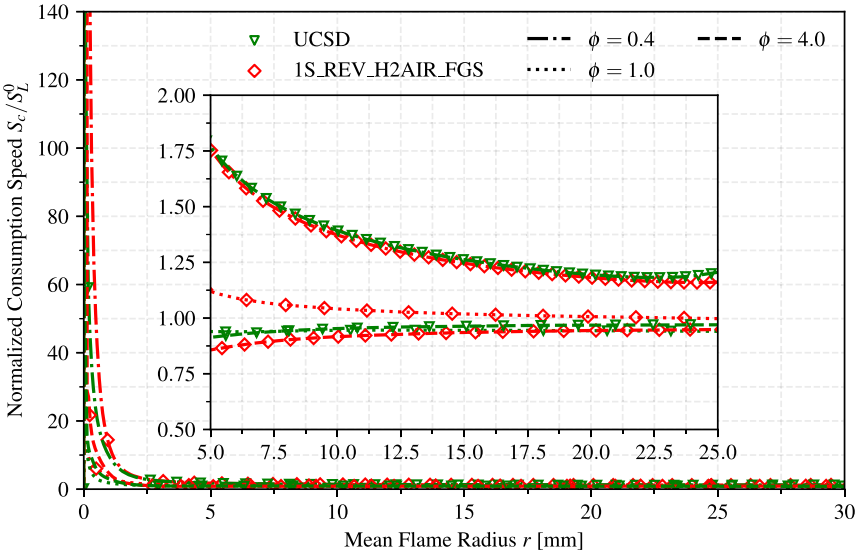

Fig. 14. Normalized consumption speed versus mean flame radius for lean ($\phi = 0.4$), stoichiometric ($\phi = 1.0$) and rich ($\phi = 4.0$) 2D cylindrical expanding flames at RTP. The inset enhances the values calculated in the domain region not affected by energy deposition ignition and outlet boundary conditions. Comparison between numerical integrations with reduced 1S_REV_H2AIR_FGS scheme and reference UCSD mechanism.

Table 5
Comparison of computational costs for reduced 1S_REV_H2AIR_FGS scheme and reference UCSD mechanism in terms of maximum computed time step Δt and iterations per second I_s. All calculations are performed with the same set-up (7.64×10^5 grid nodes, 192 CPU cores, $CFL = 0.7$, $Fo = 0.1$).

ϕ	1S_REV_H2AIR_FGS		UCSD	
	Δt [ns]	I_s [s^{-1}]	Δt [ns]	I_s [s^{-1}]
0.4	9.02	36.6	7.80	23.8
1.0	5.93	36.2	3.36	23.6
4.0	4.48	36.5	3.64	23.6

(UCSD) mechanism. It is here evident the advantage of using a one-step chemistry description in terms of computational costs, with an increase in the number of iterations per second of approximately 55% when passing from the detailed to the reduced chemistry. Moreover, the computed time step for the reduced scheme is higher than in the UCSD mechanism for all cases considered, leading to a lower number of iterations required to simulate the same physical time.

4. Conclusions

In this work, a global one-step reduced scheme, based on an Arrhenius formulation, has been derived for hydrogen-air combustion in an extended range of equivalence ratios, temperatures and pressures. The mechanism is based on analytical modeling of hydrogen oxidation to reduce the number of species, hence of transport equations to solve, in CFD codes, with a significant gain in computational efficiency.

In particular, a best-fitting methodology, based on the laminar flame speed value, has been applied to derive an explicit, analytical dependence of reaction rate parameters on equivalence ratio, system pressure, and unburned gas temperature. The Pre-Exponential Adjustment method, defined in [34], has been extended by combining the dependence on equivalence ratio with a pressure-scaling law, so that the structure of the scheme is preserved at different pressures, and the validity of the mechanism is extended to mixture conditions of interest in practical applications (e.g., gas turbine combustion). Moreover, a correction has been introduced to improve the prediction of the temperature profile in the flame reaction zone, hence of the thermal flame thickness, which is of interest for grid resolution purposes. Particular attention has been posed to separate the dependence on pressure and chemical composition in the definition of the Pre-Exponential Adjustment laws, so that the thus obtained reduced-chemistry models may be easily implemented in CFD numerical codes, allowing to obtain a sufficiently accurate estimate of the main flame properties with a reduced computational cost.

To define and validate the parameters of the reduced schemes, computations of one-dimensional unstrained and strained laminar premixed flames have been performed for a wide range of pressure ([1; 30] atm), unburned gas temperature ([300; 800] K), and equivalence ratio ([0.4; 6.0]), showing a good agreement on the prediction of main flame parameters (i.e., laminar flame speed, adiabatic flame temperature, and thermal flame thickness), in the whole range of considered mixture conditions, between the proposed reduced scheme and three reference detailed reaction mechanisms: the San Diego mechanism [22], the Konnov mechanism [38], and the H2_NOX_15_94_TC scheme [39]. Nevertheless, some limits have been found in the prediction of response to strain for stoichiometric flames, indicating potential for further optimization of the reduced scheme parameters.

The applicability of the scheme for Computational Fluid Dynamics purposes has been subsequently assessed by implementing the thus defined reduced global mechanism in the Navier–Stokes compressible DNS/LES solver AVBP (www.cerfacs.fr/avbp7x) for the computation of canonical configurations such as one-dimensional and two-dimensional premixed flames. In particular, considering a two-dimensional cylindrical expanding flame configuration, the reduced mechanism has shown a significantly good agreement with the reference San Diego mechanism in the prediction of flame structure and properties, and a sensible reduction of computational costs, both in terms of iterations per second and total number of iterations required.

The proposed global reaction mechanism aims at a practical solution to avoid computationally expensive numerical simulations of hydrogen-air combustion, especially in a preliminary design phase, optimizing computational resources by delaying the adoption of expensive detailed reaction schemes to more advanced phases of the design process. Moreover, the methodology introduced to develop the reduced mechanism is applicable to other fuels or different mixture conditions of interest, which may be expected to be the subject of further study.

Finally, in future work, the performances of the proposed 1S_REV_H2AIR_FGS scheme will be evaluated in the context of laminar diffusion and partially-premixed flames as well as of LES/DNS simulations of turbulent reactive flows, varying the operating points, so that all configurations of practical interest can be surveyed.

Declaration of competing interest

The authors declare that they have no known competing financial interests or personal relationships that could have appeared to influence the work reported in this paper.

Acknowledgments

The authors would like to acknowledge CERFACS for the grant to use the AVBP code, and the European Union's Horizon 2020 Research and Innovation Program for the financial support to N. Detomaso [Grant Agreement No. 956803 (INSPIRE - INSpiring Pressure gain combustion Integration, Research, and Education)]. This work has been supported under the National Recovery and Resilience Plan (NRRP), Mission 4 Component 2 Investment 1.4 - Call for tender No. 3138 of December 16, 2021 of the Italian Ministry of University and Research, funded by the European Union - NextGenerationEU [Award Number: CNMS named MOST, Concession Decree No. 1033 of June 17, 2022, adopted by the Italian Ministry of University and Research, CUP: D93C22000410001, Spoke 14 "Hydrogen and New Fuels"]. The computing resources and the related technical support used for part of this work have been provided by CRESCO/ENEAGRID High Performance Computing infrastructure and its staff [83]. CRESCO/ENEAGRID High Performance Computing infrastructure is funded by ENEA, the Italian National Agency for New Technologies, Energy and Sustainable Economic Development and by Italian and European research programmes, see http://www.cresco.enea.it/english for information.

Appendix A. Supplementary data

Supplementary material related to this article can be found online at https://doi.org/10.1016/j.ijhydene.2023.12.301.

References

[1] Elam CC, Padró CEG, Sandrock G, Luzzi A, Lindblad P, Hagen EF. Realizing the hydrogen future: the International Energy Agency's efforts to advance hydrogen energy technologies. Int J Hydrogen Energy 2003;28(6):601–7. http://dx.doi.org/10.1016/S0360-3199(02)00147-7.

[2] Boretti A. Green hydrogen is a necessary component of a grid with an increasing non-dispatchable renewable energy supply. Int J Hydrogen Energy 2023;48(84):32589–97. http://dx.doi.org/10.1016/j.ijhydene.2023.05.057.

[3] Kovač A, Paranos M, Marciuš D. Hydrogen in energy transition: A review. Int J Hydrogen Energy 2021;46(16):10016–35. http://dx.doi.org/10.1016/j.ijhydene.2020.11.256.

[4] Chiesa P, Lozza G, Mazzocchi L. Using hydrogen as gas turbine fuel. J Eng Gas Turbines Power 2005;127(1):73–80. http://dx.doi.org/10.1115/1.1787513.

[5] Öberg S, Odenberger M, Johnsson F. Exploring the competitiveness of hydrogen-fueled gas turbines in future energy systems. Int J Hydrogen Energy 2022;47(1):624–44. http://dx.doi.org/10.1016/j.ijhydene.2021.10.035.

[6] Verstraete D. Long range transport aircraft using hydrogen fuel. Int J Hydrogen Energy 2013;38(34):14824–31. http://dx.doi.org/10.1016/j.ijhydene.2013.09.021.

[7] Verhelst S, Turner JWG. Hydrogen-fueled spark ignition engine. In: Tingas E-A, editor. Hydrogen for future thermal engines. Cham: Springer International Publishing; 2023, p. 329–51. http://dx.doi.org/10.1007/978-3-031-28412-0_8.

[8] Dimitriou P, Tsujimura T. A review of hydrogen as a compression ignition engine fuel. Int J Hydrogen Energy 2017;42(38):24470–86. http://dx.doi.org/10.1016/j.ijhydene.2017.07.232.

[9] Capurso T, Stefanizzi M, Torresi M, Camporeale SM. Perspective of the role of hydrogen in the 21st century energy transition. Energy Convers Manage 2022;251:114898. http://dx.doi.org/10.1016/j.enconman.2021.114898.

[10] Aniello A, Poinsot T, Selle L, Schuller T. Hydrogen substitution of natural-gas in premixed burners and implications for blow-off and flashback limits. Int J Hydrogen Energy 2022;47(77):33067–81. http://dx.doi.org/10.1016/j.ijhydene.2022.07.066.

[11] Johannessen B, North A, Dibble R, Løvås T. Experimental studies of autoignition events in unsteady hydrogen–air flames. Combust Flame 2015;162(9):3210–9. http://dx.doi.org/10.1016/j.combustflame.2015.05.008.

[12] Guo L, Su J, Wang Z, Shi J, Guan X, Cao W, et al. Hydrogen safety: An obstacle that must be overcome on the road towards future hydrogen economy. Int J Hydrogen Energy 2023. http://dx.doi.org/10.1016/j.ijhydene.2023.08.248.

[13] Ma N, Zhao W, Wang W, Li X, Zhou H. Large scale of green hydrogen storage: opportunities and challenges. Int J Hydrogen Energy 2023. http://dx.doi.org/10.1016/j.ijhydene.2023.09.021.

[14] Zlochower IA, Green GM. The limiting oxygen concentration and flammability limits of gases and gas mixtures. J Loss Prev Process Ind 2009;22(4):499–505. http://dx.doi.org/10.1016/j.jlp.2009.03.006.

[15] Chen X, Liu Q, Jing Q, Mou Z, Shen Y, Huang J, et al. The characteristics of flame propagation in hydrogen/oxygen mixtures. Int J Hydrogen Energy 2022;47(17):10069–82. http://dx.doi.org/10.1016/j.ijhydene.2022.01.097.

[16] Lai J, Ahmed U, Klein M, Chakraborty N. A comparison between head-on quenching of stoichiometric methane-air and hydrogen-air premixed flames using Direct Numerical Simulations. Int J Heat Fluid Flow 2022;93:108896. http://dx.doi.org/10.1016/j.ijheatfluidflow.2021.108896.

[17] Coulon V, Gaucherand J, Xing V, Laera D, Lapeyre C, Poinsot T. Direct numerical simulations of methane, ammonia-hydrogen and hydrogen turbulent premixed flames. Combust Flame 2023;256:112933. http://dx.doi.org/10.1016/j.combustflame.2023.112933.

[18] Mauss F, Peters N, Rogg B, Williams FA. Reduced kinetic mechanisms for premixed hydrogen flames. In: Peters N, Rogg B, editors. Reduced kinetic mechanisms for applications in combustion systems. Berlin, Heidelberg: Springer; 1993, p. 29–43. http://dx.doi.org/10.1007/978-3-540-47543-9_3.

[19] Wang B, Wei W, Ma S, Wei G. Construction of one-step H2/O2 reaction mechanism for predicting ignition and its application in simulation of supersonic combustion. Int J Hydrogen Energy 2016;41(42):19191–206. http://dx.doi.org/10.1016/j.ijhydene.2016.09.010.

[20] Sánchez AL, Williams FA. Recent advances in understanding of flammability characteristics of hydrogen. Prog Energy Combust Sci 2014;41:1–55. http://dx.doi.org/10.1016/j.pecs.2013.10.002.

[21] Aniello A, Laera D, Marragou S, Magnes H, Selle L, Schuller T, et al. Experimental and numerical investigation of two flame stabilization regimes observed in a dual swirl H2-air coaxial injector. Combust Flame 2023;249:112595. http://dx.doi.org/10.1016/j.combustflame.2022.112595.

[22] Saxena P, Williams FA. Testing a small detailed chemical-kinetic mechanism for the combustion of hydrogen and carbon monoxide. Combust Flame 2006;145(1–2):316–23. http://dx.doi.org/10.1016/j.combustflame.2005.10.004.

[23] Boivin P, Jiménez C, Sánchez AL, Williams FA. An explicit reduced mechanism for H2–air combustion. Proc Combust Inst 2011;33(1):517–23. http://dx.doi.org/10.1016/j.proci.2010.05.002.

[24] Fernández-Galisteo D, Sánchez AL, Liñán A, Williams FA. One-step reduced kinetics for lean hydrogen–air deflagration. Combust Flame 2009;156(5):985–96. http://dx.doi.org/10.1016/j.combustflame.2008.10.009.

[25] Fernández-Galisteo D, Weiss A, Sánchez AL, Williams FA. A one-step reduced mechanism for near-limit hydrogen combustion with general stoichiometry. Combust Flame 2019;208:1–4. http://dx.doi.org/10.1016/j.combustflame.2019.06.018.

[26] Carpio J, Li B, Fernández-Galisteo D, Sánchez AL, Williams FA. Systematically derived one-step kinetics for hydrogen-air gas-turbine combustion. Combust Flame 2023;250:112633. http://dx.doi.org/10.1016/j.combustflame.2023.112633.

[27] Coffee TP, Kotlar AJ, Miller MS. The overall reaction concept in premixed, laminar, steady-state flames. I. Stoichiometries. Combust Flame 1983;54(1–3):155–69. http://dx.doi.org/10.1016/0010-2180(83)90029-9.

[28] Coffee TP, Kotlar AJ, Miller MS. The overall reaction concept in premixed, laminar, steady-state flames. II. Initial temperatures and pressures. Combust Flame 1984;58(1):59–67. http://dx.doi.org/10.1016/0010-2180(84)90078-6.

[29] Marinov NM, Westbrook CK, Pitz WJ. Detailed and global chemical kinetics model for hydrogen. In: Chan SH, editor. Transport phenomena in combustion, vol. 1. Washington D.C.: Taylor & Francis; 1996, p. 118–29.

[30] Wang C, Wen J, Lu S, Guo J. Single-step chemistry model and transport coefficient model for hydrogen combustion. Sci China Technol Sci 2012;55:2163–8. http://dx.doi.org/10.1007/s11431-012-4932-4.

[31] Bane S, Ziegler J, Shepherd J. Development of one-step chemistry models for flame and ignition simulation. Technical report FM2010-002, Graduate Aeronautical Laboratories, California Institute of Technology; 2010.

[32] Bar-Kohany T, Dahan K. Evaluation of the one-step hydrogen–oxygen global reaction rate in a non-premixed mixture to predict auto-ignition limits. Int J Hydrogen Energy 2012;37(19):14669–75. http://dx.doi.org/10.1016/j.ijhydene.2012.07.017.

[33] Kim HY, Kim NI. Optimized global reaction mechanisms for H2, CO, CH4, and their mixtures. Int J Hydrogen Energy 2023;48(62):24101–12. http://dx.doi.org/10.1016/j.ijhydene.2023.03.189.

[34] Franzelli B, Riber E, Gicquel LY, Poinsot T. Large eddy simulation of combustion instabilities in a lean partially premixed swirled flame. Combust Flame 2012;159(2):621–37. http://dx.doi.org/10.1016/j.combustflame.2011.08.004.

[35] Law CK, Sung CJ. Structure, aerodynamics, and geometry of premixed flamelets. Prog Energy Combust Sci 2000;26(4–6):459–505. http://dx.doi.org/10.1016/S0360-1285(00)00018-6.

[36] Law CK. Propagation, structure, and limit phenomena of laminar flames at elevated pressures. Combust Sci Technol 2006;178(1–3):335–60. http://dx.doi.org/10.1080/00102200500290690.

[37] Goodwin DG, Moffat HK, Speth RL. Cantera: An Object-oriented Software Toolkit for Chemical Kinetics, Thermodynamics, and Transport Processes. 2017, http://dx.doi.org/10.5281/zenodo.170284, Version 2.3.0, https://www.cantera.org.

[38] Konnov AA. Yet another kinetic mechanism for hydrogen combustion. Combust Flame 2019;203:14–22. http://dx.doi.org/10.1016/j.combustflame.2019.01.032.

[39] Capurso T, Laera D, Riber E, Cuenot B. NOx pathways in lean partially premixed swirling H2-air turbulent flame. Combust Flame 2023;248:112581. http://dx.doi.org/10.1016/j.combustflame.2022.112581.

[40] Ranzi E, Frassoldati A, Stagni A, Pelucchi M, Cuoci A, Faravelli T. Reduced kinetic schemes of complex reaction systems: fossil and biomass-derived transportation fuels. Int J Chem Kinet 2014;46(9):512–42. http://dx.doi.org/10.1002/kin.20867.

[41] Sun CJ, Sung CJ, He L, Law CK. Dynamics of weakly stretched flames: quantitative description and extraction of global flame parameters. Combust Flame 1999;118(1–2):108–28. http://dx.doi.org/10.1016/S0010-2180(98)00137-0.

[42] Egolfopoulos FN, Law CK. Chain mechanisms in the overall reaction orders in laminar flame propagation. Combust Flame 1990;80(1):7–16. http://dx.doi.org/10.1016/0010-2180(90)90049-W.

[43] Poinsot T, Veynante D. Theoretical and numerical combustion. RT Edwards, Inc.; 2005.

[44] Konnov AA, Mohammad A, Kishore VR, Kim NI, Prathap C, Kumar S. A comprehensive review of measurements and data analysis of laminar burning velocities for various fuel+air mixtures. Prog Energy Combust Sci 2018;68:197–267. http://dx.doi.org/10.1016/j.pecs.2018.05.003.

[45] Butler T, O'Rourke P. A numerical method for two dimensional unsteady reacting flows. Symp (Int) Combust 1977;16(1):1503–15. http://dx.doi.org/10.1016/S0082-0784(77)80432-3.

[46] Dixon-Lewis G. Flame structure and flame reaction kinetics II. Transport phenomena in multicomponent systems. Proc R Soc A 1968;307(1488):111–35. http://dx.doi.org/10.1098/rspa.1968.0178.

[47] Grcar JF, Bell JB, Day MS. The Soret effect in naturally propagating, premixed, lean, hydrogen–air flames. Proc Combust Inst 2009;32(1):1173–80. http://dx.doi.org/10.1016/j.proci.2008.06.075.

[48] Sánchez AL, Williams FA. Corrigendum to "Recent advances in understanding of flammability characteristics of hydrogen". Prog Energy Combust Sci 2016;54:93–4. http://dx.doi.org/10.1016/j.pecs.2016.04.001.

[49] Dowdy DR, Smith DB, Taylor SC, Williams A. The use of expanding spherical flames to determine burning velocities and stretch effects in hydrogen/air mixtures. Symp (Int) Combust 1991;23(1):325–32. http://dx.doi.org/10.1016/S0082-0784(06)80275-4.

[50] Egolfopoulos F, Law C. An experimental and computational study of the burning rates of ultra-lean to moderately-rich H2/O2/N2 laminar flames with pressure variations. Symp (Int) Combust 1991;23(1):333–40. http://dx.doi.org/10.1016/S0082-0784(06)80276-6.

[51] Vagelopoulos C, Egolfopoulos F, Law C. Further considerations on the determination of laminar flame speeds with the counterflow twin-flame technique. Symp (Int) Combust 1994;25(1):1341–7. http://dx.doi.org/10.1016/S0082-0784(06)80776-9.

[52] Karpov VP, Lipatnikov AN, Wolanski P. Finding the Markstein number using the measurements of expanding spherical laminar flames. Combust Flame 1997;109(3):436–48. http://dx.doi.org/10.1016/S0010-2180(96)00166-6.

[53] Tse SD, Zhu DL, Law CK. Morphology and burning rates of expanding spherical flames in H2/O2/inert mixtures up to 60 atmospheres. Proc Combust Inst 2000;28(2):1793–800. http://dx.doi.org/10.1016/S0082-0784(00)80581-0.

[54] Kwon OC, Faeth GM. Flame/stretch interactions of premixed hydrogen-fueled flames: measurements and predictions. Combust Flame 2001;124(4):590–610. http://dx.doi.org/10.1016/S0010-2180(00)00229-7.

[55] Lamoureux N, Djebaıli-Chaumeix N, Paillard C-E. Laminar flame velocity determination for H2–air–He–CO2 mixtures using the spherical bomb method. Exp Therm Fluid Sci 2003;27(4):385–93. http://dx.doi.org/10.1016/S0894-1777(02)00243-1.

[56] Verhelst S, Woolley R, Lawes M, Sierens R. Laminar and unstable burning velocities and markstein lengths of hydrogen–air mixtures at engine-like conditions. Proc Combust Inst 2005;30(1):209–16. http://dx.doi.org/10.1016/j.proci.2004.07.042.

[57] Burke MP, Chen Z, Ju Y, Dryer FL. Effect of cylindrical confinement on the determination of laminar flame speeds using outwardly propagating flames. Combust Flame 2009;156(4):771–9. http://dx.doi.org/10.1016/j.combustflame.2009.01.013.

[58] Kuznetsov M, Kobelt S, Grune J, Jordan T. Flammability limits and laminar flame speed of hydrogen–air mixtures at sub-atmospheric pressures. Int J Hydrogen Energy 2012;37(22):17580–8. http://dx.doi.org/10.1016/j.ijhydene.2012.05.049.

[59] Krejci MC, Mathieu O, Vissotski AJ, Ravi S, Sikes TG, Petersen EL, et al. Laminar flame speed and ignition delay time data for the kinetic modeling of hydrogen and syngas fuel blends. J Eng Gas Turbines Power 2013;135(2). http://dx.doi.org/10.1115/1.4007737.

[60] Dahoe AE. Laminar burning velocities of hydrogen–air mixtures from closed vessel gas explosions. J Loss Prev Process Ind 2005;18(3):152–66. http://dx.doi.org/10.1016/j.jlp.2005.03.007.

[61] Bradley D, Lawes M, Liu K, Verhelst S, Woolley R. Laminar burning velocities of lean hydrogen–air mixtures at pressures up to 1.0 MPa. Combust Flame 2007;149(1–2):162–72. http://dx.doi.org/10.1016/j.combustflame.2006.12.002.

[62] Matalon M. The Darrieus–Landau instability of premixed flames. Fluid Dyn Res 2018;50(5):051412. http://dx.doi.org/10.1088/1873-7005/aab510.

[63] Matalon M, Cui C, Bechtold J. Hydrodynamic theory of premixed flames: effects of stoichiometry, variable transport coefficients and arbitrary reaction orders. J Fluid Mech 2003;487:179–210. http://dx.doi.org/10.1017/S0022112003004683.

[64] Howarth T, Aspden A. An empirical characteristic scaling model for freely-propagating lean premixed hydrogen flames. Combust Flame 2022;237:111805. http://dx.doi.org/10.1016/j.combustflame.2021.111805.
[65] Howarth T, Hunt E, Aspden A. Thermodiffusively-unstable lean premixed hydrogen flames: Phenomenology, empirical modelling, and thermal leading points. Combust Flame 2023;253:112811. http://dx.doi.org/10.1016/j.combustflame.2023.112811.
[66] Skottene M, Rian KE. A study of NOx formation in hydrogen flames. Int J Hydrogen Energy 2007;32(15):3572–85. http://dx.doi.org/10.1016/j.ijhydene.2007.02.038.
[67] Hawkes ER, Chen JH. Comparison of direct numerical simulation of lean premixed methane–air flames with strained laminar flame calculations. Combust Flame 2006;144(1–2):112–25. http://dx.doi.org/10.1016/j.combustflame.2005.07.002.
[68] Franzelli B, Riber E, Cuenot B. Impact of the chemical description on a Large Eddy Simulation of a lean partially premixed swirled flame. C R Méc 2013;341(1–2):247–56. http://dx.doi.org/10.1016/j.crme.2012.11.007.
[69] Detomaso N, Hok J-J, Dounia O, Laera D, Poinsot T. A generalization of the Thickened Flame model for stretched flames. Combust Flame 2023;258:113080. http://dx.doi.org/10.1016/j.combustflame.2023.113080.
[70] Lax P, Wendroff B. Systems of conservation laws. Technical report, Los Alamos, NM (United States): Los Alamos National Laboratory (LANL); 1958, http://dx.doi.org/10.2172/4244712.
[71] Colin O, Rudgyard M. Development of High-Order Taylor–Galerkin Schemes for LES. J Comput Phys 2000;162(2):338–71. http://dx.doi.org/10.1006/jcph.2000.6538.
[72] Poinsot TJ, Lele SK. Boundary Conditions for Direct Simulations of Compressible Viscous Flows. J Comput Phys 1992;101(1):104–29. http://dx.doi.org/10.1016/0021-9991(92)90046-2.
[73] Granet V, Vermorel O, Léonard T, Gicquel L, Poinsot T. Comparison of Nonreflecting Outlet Boundary Conditions for Compressible Solvers on Unstructured Grids. AIAA J 2010;48(10):2348–64. http://dx.doi.org/10.2514/1.J050391.
[74] Lacaze G, Richardson E, Poinsot T. Large eddy simulation of spark ignition in a turbulent methane jet. Combust Flame 2009;156(10):1993–2009. http://dx.doi.org/10.1016/j.combustflame.2009.05.006.
[75] Law CK. Combustion physics. Cambridge University Press; 2006, http://dx.doi.org/10.1017/CBO9780511754517.
[76] Berger L, Attili A, Pitsch H. Intrinsic instabilities in premixed hydrogen flames: Parametric variation of pressure, equivalence ratio, and temperature. Part 1 - Dispersion relations in the linear regime. Combust Flame 2022;240:111935. http://dx.doi.org/10.1016/j.combustflame.2021.111935.
[77] Bechtold J, Matalon M. Hydrodynamic and diffusion effects on the stability of spherically expanding flames. Combust Flame 1987;67(1):77–90. http://dx.doi.org/10.1016/0010-2180(87)90015-0.
[78] Xin YX, Yoo CS, Chen JH, Law CK. A DNS study of self-accelerating cylindrical hydrogen–air flames with detailed chemistry. Proc Combust Inst 2015;35(1):753–60. http://dx.doi.org/10.1016/j.proci.2014.06.076.
[79] Giannakopoulos GK, Frouzakis CE, Mohan S, Tomboulides AG, Matalon M. Consumption and displacement speeds of stretched premixed flames-theory and simulations. Combust Flame 2019;208:164–81. http://dx.doi.org/10.1016/j.combustflame.2019.06.027.
[80] Kelley AP, Law CK. Nonlinear effects in the extraction of laminar flame speeds from expanding spherical flames. Combust Flame 2009;156(9):1844–51. http://dx.doi.org/10.1016/j.combustflame.2009.04.004.
[81] Bray KNC. Studies of the turbulent burning velocity. Proc R Soc A 1990;431(1882):315–35. http://dx.doi.org/10.1098/rspa.1990.0133.
[82] Gaucherand J, Laera D, Schulze-Netzer C, Poinsot T. Intrinsic instabilities of hydrogen and hydrogen/ammonia premixed flames: Influence of equivalence ratio, fuel composition and pressure. Combust Flame 2023;256:112986. http://dx.doi.org/10.1016/j.combustflame.2023.112986.
[83] Iannone F, Ambrosino F, Bracco G, De Rosa M, Funel A, Guarnieri G, et al. CRESCO ENEA HPC clusters: a working example of a multifabric GPFS Spectrum Scale layout. In: 2019 International conference on high performance computing & simulation. IEEE; 2019, p. 1051–2. http://dx.doi.org/10.1109/HPCS48598.2019.9188135.